Fatigue performance of laser powder bed fusion hydride-dehydride Ti-6Al-4V powder

Mohammadreza Asherloo ^a, Ziheng Wu ^b, Mike Heim ^c, Dave Nelson ^c, Muktesh Paliwal ^d, Anthony D. Rollett ^e, Amir Mostafaei ^{a, *}

- ^a Department of Mechanical, Materials and Aerospace Engineering, Illinois Institute of Technology, 10 W 32nd Street, Chicago, IL 60616, USA
- ^b Materials Engineering Division, Lawrence Livermore National Laboratory, 7000 East Ave, Livermore, CA 94550
- ^c Nel Pretech Corporation, 8420 183rd Place, Tinley Park, IL 60487, USA
- ^d Kymera International Reading Alloys, Robesonia, PA 19551, USA
- ^e Department of Materials Science and Engineering, Carnegie Mellon University, Pittsburgh, PA, 15213, USA
- * Corresponding authors: A. Mostafaei (mostafaei@iit.edu)

Abstract

Hydride-dehydride (HDH) Ti-6Al-4V alloy with particle size distribution of 50-120 μm is laser powder bed fusion (L-PBF) processed using optimum processing parameters and a near-fully dense structure with a density of 99.9 % is achieved. Microstructural observations and phase analyses indicate formation of columnar β grains with acicular α/α' phases in as-built condition. The roughness of the as-fabricated samples is significant with an average roughness of R_a = $15.71\pm3.96 \,\mu\text{m}$ and a root mean square roughness of $R_{rms} = 108.4\pm24.9 \,\mu\text{m}$, however, both values are reduced to $R_a = 0.19 \pm 0.04 \, \mu \text{m}$ and $R_{rms} = 4.9 \pm 0.6 \, \mu \text{m}$ after mechanical grinding. Mechanical tests are carried out on as-fabricated specimens followed by stress relief treatment. All samples are tested to failure in fatigue, under fully-reversed tension-compression conditions of R = -1. The asbuilt samples failed from the surface with crack initiation mainly at micro-notches, whereas after mechanically grinding, crack initiation changed to subsurface defects such as pores. Minimizing surface roughness by mechanically grinding eliminates surface micro-notches which improves fatigue strength in the high cycle fatigue region. Fatigue notch factor calculations showed that the effect of surface roughness was significantly lower when HDH powder is used compared to standard spherical powder. X-ray diffraction analysis revealed an in-plane compressive stress, micro-strain and grain refinement on the surface of the mechanically ground samples. Fractography observations (macroscale) revealed a fully brittle fracture in the first stage of crack growth with a transition to a dominantly ductile fracture in in the third stage of crack growth. On the other hand, at the micro scale, even the brittle fracture regions showed evidence of ductile fracture within the α' martensite laths.

Keywords: Additive manufacturing; non-spherical powder; Surface roughness; Fractography; Micro-computed tomography.

1. Introduction

Spherical powder produced by gas atomization (GA) has been the dominant type of powder being used in powder bed fusion additive manufacturing (AM), such as laser powder bed fusion (L-PBF) and electron beam powder bed fusion (EB-PBF) [1,2]. However, the spherical powder raises a number of concerns for powder bed fusion AM. Firstly, the production of spherical powders is highly energy-intensive due to energy needed for melting the alloy; for reactive materials, the requirements of an inert environment to prevent oxidation under high-temperature conditions adds to the production costs. Atomization may also not be an appropriate method to produce powder for high-temperature [3] and shape memory alloys [4,5]. In addition, the entrapment of gas pores inside the atomized particles can transfer porosity into the final part and

degrade the resulting mechanical performance especially under fatigue loading [6–9]. Finally, the cost of powder production also contributes to the overall manufacturing cost of AM, thus, production of a high-quality, low-cost powder seems essential for viability of metal AM processes.

In order to mitigate challenges related to production of metal powder, alternative production methods should be investigated. Hydride-dehydride (HDH) process is an alternative method for producing titanium alloy powders where the final product is in non-spherical shape [10]. There are several aspects of using a non-spherical powder that motivate research, such as melt pool dynamics, possible new defect formation mechanisms and physics of laser-powder interaction, all of which can be affected by the non-spherical powder morphology. First, pore-free powder produced by HDH method eliminates issues associated with the entrapped gas bubbles transferred to the final L-PBF processed parts from feedstock [11]. Also, shape and size of powder potentially minimize spattering issue based on mechanical interlocking and higher mass of the used HDH powder compared to the fine spherical powder with PSD of 20-60 μm . However, the morphology of the non-spherical powder makes size control more challenging. It is also believed that the flowability and packing density of non-spherical powders are lower than the GA powders. Asherloo et al. [12] showed that the powder packing density of GA powder with particle size distribution of 20-63 μm was ~ 58 %, while, it was ~ 55 % in non-spherical powder with a particle size distribution of 50-120 μm .

Recently, studies have been conducted on the use of non-spherical powders in powder bed fusion AM. Narra et al. [13] investigated the use of HDH Ti-6Al-4V powder in EB-PBF process by following a processing parameters optimization approach and concluded that a relative density >99 % is achievable. Wu et al. [14] successfully L-PBF processed non-spherical HDH Ti-6Al-4V powder to fabricate parts with relative density up to 99.8 %. They also reported the possibility of powder spreading giving rise to patches of low packing density which would enhance formation of non-continuous melt pool tracks during laser processing. In other words, a lowdensity site in spread powder layer might lead to the formation of a cavity on the melted surface. The next layer of powder to be spread would then have a locally thicker powder layer in the cavity which might not be fully melted by the laser which in turn would generate a lack-of-fusion pore. Medina [15] EB-PBF processed HDH powder with various ratios in the range 25-100 % of nonspherical to spherodized particles. He showed that when optimum process parameters were applied, a relative density of >99 % was achieved using a mixed powder containing 25 % non-spherical particles. Jaber et al. [16] used a hybrid powder consisting of a 50-50 mix of plasma atomized (PA) and HDH powder to increase the cost efficiency while preserving the desirable characteristics of the PA powder. However, they concluded that this resulted in significantly lower yield stress and elongation. On the other hand, Varela et al. [17] used various heat treatment processes to mitigate the effect of HDH powder irregularity on the final properties of the parts.

Fatigue performance of additively manufactured Ti-6Al-4V parts is lower than the wrought parts because of surface roughness, porosity, and residual stress [18], thus, it is necessary to control each of these features to enhance fatigue performance. Gong et al. [19] evaluated the effect of defect size and geometry on the fatigue life of the L-PBF processed Ti-6Al-4V. In the low cycle fatigue region (at stresses higher than 500 MPa), crack initiation occurred on the surface regardless of presence or absence of defects (mainly pores) in the bulk, whereas high cycle fatigue was influenced by the shape and size of internal defects. Cain et al. [20] found that the fatigue crack growth rate decreased when the as-built L-PBF Ti-6Al-4V specimens were subjected to stress relief treatment at 650 °C for 4 h. Pegues et al. [21] studied the effect of surface finish on fatigue

performance and found that when polishing decreased the surface roughness from $31.41~\mu m$ to $0.45~\mu m$, the fatigue strength at 1,000 cycles increased from 75 MPa in the as-built condition to 450~MPa as polished. Thus, it is obvious that the combination of internal defects and surface finish play a crucial role on performance of AM parts. This could be a potential challenge when non-spherical powders are used in powder bed fusion AM processes [22].

In this study, the fatigue performance of samples fabricated using HDH Ti-6Al-4V powder in two conditions, as-built and mechanically ground, was investigated using microstructure observation, surface characterizations such as residual stress measurement and roughness and finally fractography on the fatigue fracture surfaces to characterize crack initiation in relation to surface roughness. Comparison with parts produced with spherical powder (data collected from literature) showed that the cost-effective, non-spherical HDH powders used in this study are a viable feedstock for the L-PBF process.

2. Experimental procedures

2.1 Feedstock powder

Hydride-dihydride (HDH) Ti-6Al-4V powder with non-spherical morphology (see Figure 1) and average circularity of 0.68 was supplied by Kymera International – Reading Alloys. The nominal composition of Ti-6Al-4V and the used HDH powder are given in Table 1. Powder morphology was assessed using scanning electron microscopy (JEOL 5900LV). The particle size distribution (PSD) reported by the manufacturer was 50-120 μ m which was confirmed based on image analysis (using ImageJ software) on ~1100 particles obtained using an FEI Aspex Express SEM. This revealed a bimodal size distribution with particle size of $d_{10} = 28 \mu m$, $d_{50} = 83 \mu m$ and $d_{90} = 103 \mu m$ and a mean size of 76 μ m, Figure 1. Here, number-based statistics are presented, i.e., not weighted by particle volume.

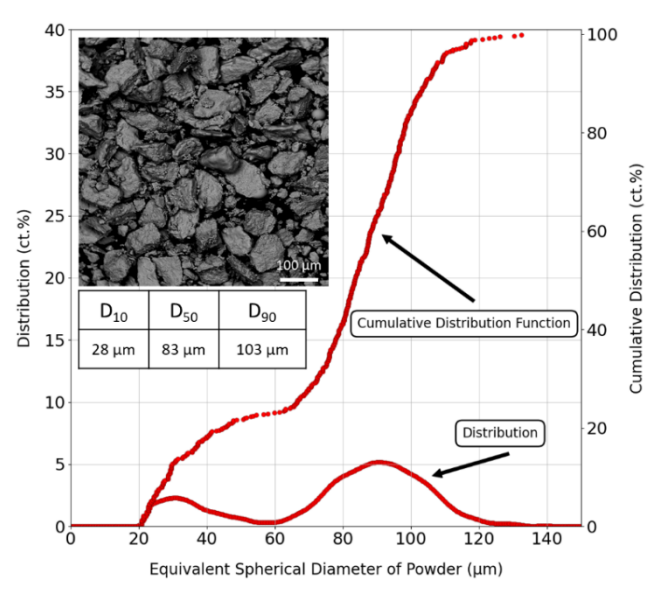


Figure 1. Particle size distribution analysis based on image processing on collected SEM micrographs taken from HDH Ti-6Al-4V powder. The inset SEM micrograph represented the morphology of the powder.

Table 1. Comparison between the nominal chemical composition of Ti-6Al-4V powder and used HDH in this study. Units are in [wt. %].

Ti	A1	V	Fe	\mathbf{C}	H	N	0
11	7 4 1	•	1 0)	**	- 1	0

Nominal composition based on	Bal.	5.5-6.75	3.5-4.5	< 0.40	< 0.08	< 0.015	< 0.05	< 0.20
ASTM B 348 standard [23]								
HDH Ti-6Al-4Vpowder	Bal.	6.08	3.88	0.19	0.02	0.005	0.02	0.17

2.2 Laser-beam powder bed fusion

The L-PBF specimens were fabricated in an EOS M290 machine. The optimum process parameters leading to a density of >99.9 % were reported previously [12] and are summarized in Table 2. Here, cubic coupons with dimensions of $15 \times 10 \times 10$ mm³ were printed for density measurements and microscopy observations. Fatigue specimens with the given dimensions and build layouts (see Figure 2A-B) were fabricated using the optimum processing parameters followed by stress-relief treatment at 650 °C for 2 h under Ar atmosphere. A wire electrical discharge machining tool (model GF machining solutions AC progress VP3 wire EDM machine) was used to remove L-PBF parts from the base plate. The gauge section surface of a number of samples was mechanically ground using a Dremel tool followed by grinding with 400, 600 and 800 grit size silicon sandpapers to ensure a good surface finish and reduction of surface roughness. Figure 2C shows the samples before and after the mechanical grinding process.

Table 2. Optimum processing parameters used for manufacturing of cubic coupons and fatigue specimens.

Power (W)	370
Scan speed (mm/s)	1250
Hatch spacing (µm)	90
Layer thickness (µm)	60
Scan rotation (°)	67
Scan strategy	Using parallel stripes scanning strategy
contour 1	190 W, 1200 mm/s, 0.03 mm inward offset
contour 2	190 W, 1250 mm/s, no inward offset

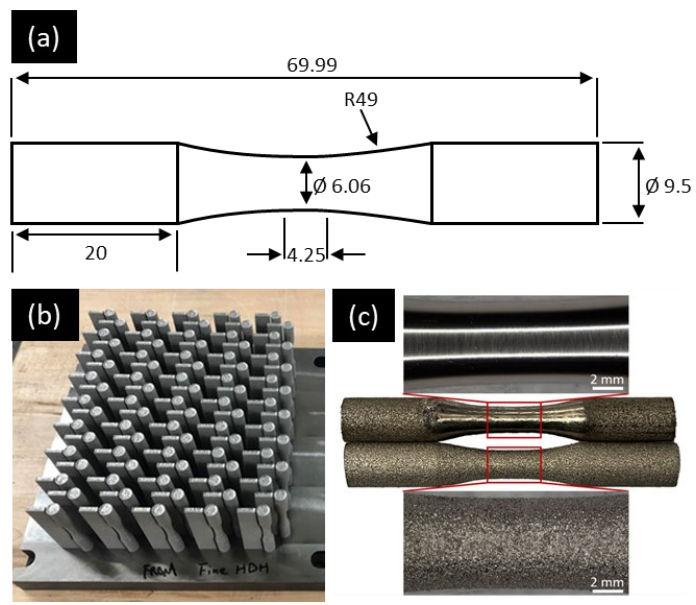


Figure 2. (A) Schematic of the fatigue specimen showing dimensions (all measurements in mm), (B) optical photograph showing layout of fatigue samples manufactured by the L-PBF process of HDH Ti-6Al-4V powder and (C) optical images of fatigue samples in the as-built (bottom) and machined (top) conditions.

2.3 Characterization of Microstructure

To observe the microstructure, metallographic preparation consisted of grinding with sandpapers with 320, 600, 800, 1200, and 2400 grit size and polishing using one micron Alumina solution and the polished surface was etched using Kroll's reagent (92 ml distilled water, 6 ml HNO₃ and 2 ml HF). Microscopy was performed using a Keyence digital microscope (model VHX 7100) and field emission scanning electron microscope (FESEM, JEOL JSM-6701F). Electron Back Scatter Diffraction (EBSD) analysis was conducted to obtain texture and detailed microstructure of the AM parts. For EBSD analysis, an SEM microscope (JEOL 5900LV) equipped with an Oxford Instruments EBSD detector was utilized operating at an acceleration voltage of 20 keV and step size of 0.3 μm. The data was collected using the AzTec software and analyzed using the HKL Channel 5 software package. The reconstruction of prior β grains was done using MTEX, an open source MATLAB-based toolbox [24]. Surface roughness was measured using an optical profiler (Keyence VHX 7100 digital microscope) on eight different positions around the gauge section of the fatigue samples.

2.4 Fatigue life assessment

Fatigue specimens were tested in air using an MTS 880 machine with a uniaxial sinusoidal cyclic loading with a stress ratio of R = -1 and a frequency of f = 30 Hz. Characterization of fracture surfaces was conducted using scanning electron microscopy. X-ray diffraction pattern analysis (XRD) was performed on samples' curved surfaces using an x-ray diffractometer (model Thermo ARL) with Cu-K α radiation ($\lambda = 1.5406$ Å, 35 kV and 30 mA), a 2θ ranging between 30-100°, a scan speed of 1 s/step, and scan step of 0.02 ° at an ambient temperature. Possible phases and crystallography parameters (peak positions, phases, and lattice parameters) were analyzed using the Powder Diffraction File database [25] and the Rietveld refinement was conducted using the MAUD [26] software.

2.5 Micro-computed tomography

Micro-computed tomography (μ -CT) was performed on the 10 mm of the gauge section of the as-built and mechanically ground samples using a Zeiss Merotom 800 system which utilized x-rays with 85 kV and 47 mA and final spatial resolution of 5.4 μ m/pixel. The μ -CT data was then post processed and visualized by VGSTUDIO software and the porosity content of the parts were extracted and normalized by the parts' volume.

3. Results and Discussion

3.1 Microstructure observations

Microstructures of the L-PBF HDH Ti-6Al-4V powder are shown in Figure 3. Detailed discussion on porosity formation as a function of laser power and scan speed can be found in our earlier study [12]. In the current study, optimum process parameters were used to fabricate parts with a relative density of 99.9 %. In this case, residual pores during fabrication could be formed because of keyholing or possible fluctuation of packing density of the powder bed [14]. Typically, the L-PBF processed Ti-6Al-4V alloy results in the formation of columnar prior β grains that are parallel to the build direction as shown in optical micrograph in Figure 3a. The high cooling rate of the L-PBF process causes diffusionless transformation of beta (β) to accicular α' martensite. Also, since the martensite finish temperature (M_f) lies below room temperature [27] as well as heat cycles during consecutive layer deposition, there are β nano-particles in the microstructure as

shown in SEM micrograph in Figure 3(a3) and Figure 3(b3) which is consistent with observations reported in [28].

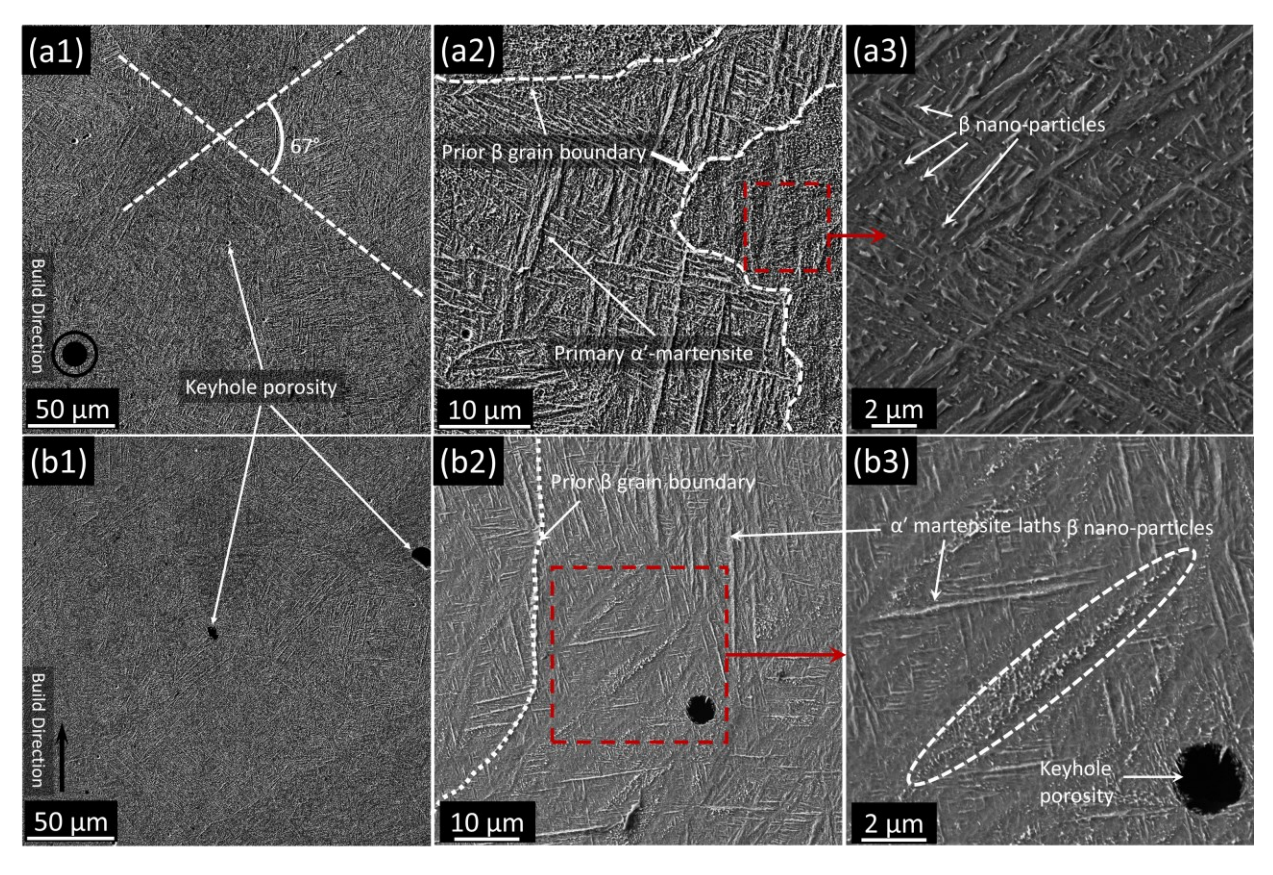


Figure 3. Scanning electron micrographs of (a) horizontal and (b) vertical cross-sections of L-PBF processed HDH Ti-6Al-4V HDH powder. Different magnifications indicated details of phases presented on horizontal or vertical cross-sections.

To further investigate the microstructure and texture of L-PBF processed HDH Ti-6Al-4V powder, microscopy observations were carried out on the vertical and horizontal cross-sections and the results are shown in Figure 4. Both optical micrograph and EBSD inverse pole figure (IPF-Z) map of the vertical cross-section showed columnar grains along the build direction due to repetitive remelting and resolidification during printing. Several studies have shown strong <100> texture of prior β grains along the build direction by using laser scan rotations of 0° or 90° [29–31], however, in the present study, the texture of the prior β grains was more random because of using 67° laser scan rotation that changes the temperature gradient directions between each successive new layer and decreases the tendency for columnar extension of previous grains during the L-PBF process.

Reconstruction of the prior β grain structure was done on both vertical and horizontal cross-sections of the L-PBF parts to better define the effect of scan rotation on the prior β grain regrowth and elongation. The reconstruction of the prior β grains was performed in the MTEX software using (1) Burgers orientation relationship between martensite (child) and prior β (parent) grains i.e., $[0001]_{\alpha} \parallel [110]_{\beta}$ and $[2\ \bar{1}\ \bar{1}\ 0]_{\alpha} \parallel [\bar{1}\ 1\ \bar{1}]_{\beta}$, (2) a minimum misorientation of 2.5°, and (3) the triple point junction method to determine the common prior β grain for different child grains [32]:

the results are shown in Figure 4(a₃,b₃). As mentioned above, the applied 67° laser scan rotation effectively interrupts epitaxial growth of the prior β grains, however, melt pool instability and non-uniform thermal gradients [33] can also result in new orientations, known as stray grains [34]. Grain boundary distortion occurs because of higher laser scan speed which causes higher temperature at the edges of the melt pool compared to the inner parts and eventually distortions of epitaxial growth of the grains [35].

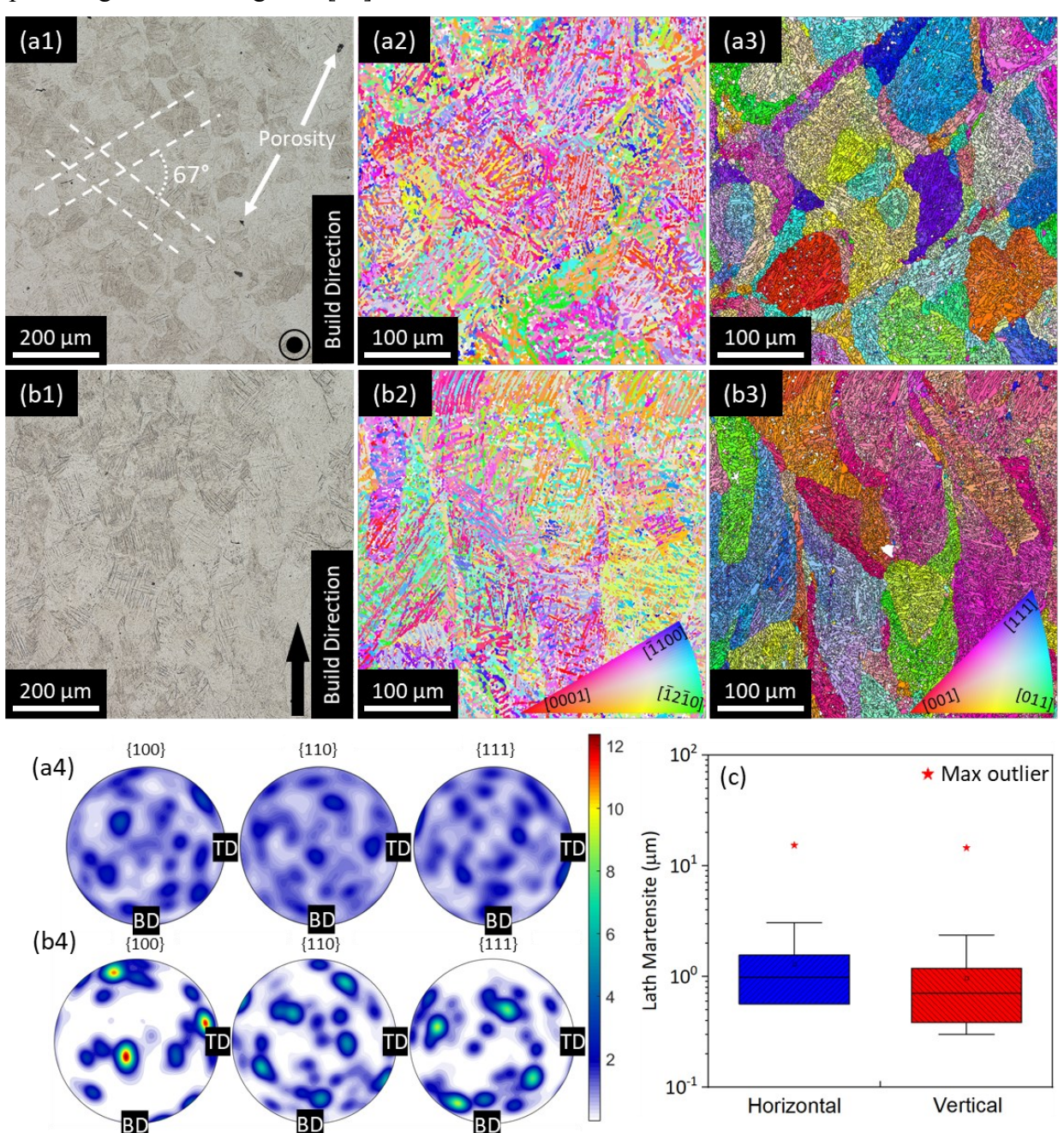


Figure 4. (a_1,b_1) Optical micrographs, (a_2,b_2) EBSD maps, (a_3,b_3) reconstructed prior β grains, and (a_4,b_4) pole figures of (a) horizontal and (b) vertical cross-sections of the L-PBF processed HDH Ti-6Al-4V powder. (c) Martensite lath size box plot of horizontal and vertical cross-sections measured using EBSD maps. Pole figures were extracted from the reconstructed prior β grains maps. BD and TD in pole figures indicate the build direction and transverse direction, respectively.

Figure 4(a4,b4) shows the pole figure data extracted from the reconstructed prior β grains on the EBSD maps. The pole figures show random texture in horizontal cross-section and relatively strong texture along <100> direction in vertical cross-section. It is worth noting that the anisotropic characteristics of the L-PBF HDH Ti-6Al-4V parts were slightly mitigated using 67° laser scan rotation compared to the parts typically printed by 0° or 90° laser scan rotation showing almost entirely columnar grains without growth interruptions [36]. Phase fraction analysis on the EBSD scans revealed about 2.3 % of β phase, in agreement with reported values for the as-built L-PBF Ti-6Al-4V alloy [37,38]. Finally, martensite lath width measured on the EBSD IPF-Z maps are shown in Figure 4c. The mean martensite lath width was 1.05 \pm 0.22 μ m.

3.2 Fatigue performance

The fatigue test results of L-PBF processed HDH Ti-6Al-4V powder in the as-built and mechanically ground conditions are shown in Figure 5 along with reference data for Ti-6Al-4V parts produced from spherical powder [38–41] and wrought alloy [42]. The Basquin equation [43] was used to fit the fatigue data of the as-built and mechanically ground specimens:

$$\sigma_a = \sigma_f'(2N_f)^b \tag{Eq. 1}$$

where σ_a is the stress amplitude, N_f is the number of cycles before failure, σ_f' is the fatigue strength coefficient, and b is the fatigue strength exponent. Based on this equation, a smaller b value for a given σ_f' corresponds to less dependence on stress amplitude and longer fatigue life [44]. All datasets are well fit with $R^2 > 0.87$ and the results are summarized in Table 3.

Table 3. Fitted fatigue strength coefficient (σ'_f) , fatigue strength exponent (b), and calculated fatigue strength at 1000 cycles (σ'_a) using Basquin equation.

	σ_f' [MPa]	b
As-built - L-PBF - HDH	8609.4	-0.29
Mechanically ground - L-PBF - HDH	2401.2	-0.161
Benedetti [40] - L-PBF - Spherical	1991.0	-0.155
Gong [41] - L-PBF - Spherical	12617.8	-0.305
Pegues [39] - L-PBF - Spherical	66755.9	-0.5
Soltani [38] - L-PBF - Spherical	12073.7	-0.3
Morissey [42] - Wrought	2472.9	-0.139

The fatigue limit of wrought Ti-6Al-4V has been extensively studied and reported to be in the range of 550-750 MPa [45], however, the fatigue limit of the samples being investigated in this study falls within 150-200 MPa, which is much lower. There are three main reasons for this stark contrast between wrought and L-PBF parts; (i) high surface roughness caused by L-PBF processing introduces intrusion sites on the surface of the AM parts that act as crack nucleation sites [46], (ii) defects and porosities introduced in the part by the L-PBF process can act as stress concentration sites and be detrimental to the mechanical properties, and (iii) the presence of a predominantly martensitic microstructure in the as-built parts is detrimental to fatigue behavior in Ti-6Al-4V as reported by Lin et al. [47]. Sanaei et al. [48] studied the fatigue performance of the powder bed fusion processed Ti-6Al-4V alloy and concluded that martensitic microstructure in L-PBF processed alloy decreases the fatigue life of the parts compared to lamellar microstructure

attained using EB-PBF process. This is attributed to the reduced ductility by the martensitic microstructure, and consequently, the higher sensitivity of the fatigue life to the critical defect size.

Although there is a substantial difference between the reference data and experimental results of this study in terms of the frequency of cyclic loading, Boyce et al. [49] concluded that frequency has a negligible effect on the crack growth rate in Ti-6Al-4V alloy regardless of the temperature and frequency range and that crack growth rate is effectively frequency-independent. By comparing fatigue results of the as-built and mechanically ground specimens, it is evident that the fatigue life slightly increases after machining the parts and removing the surface roughness (Figure 7c). This comparison is consistent with the fact that surface roughness plays an important role in crack nucleation and the higher the surface roughness, the lower the fatigue life of the parts. Moreover, mechanical grinding of the surface results in compressive residual stress on the surface of the parts, as will be discussed later, that results in even higher fatigue life compared to as-built condition. Parts printed using HDH Ti-6Al-4V powder showed relatively similar fatigue behavior compared to those fabricated by spherical powder.

Pegues et al. [39] investigated the effect of surface roughness on fatigue behavior of L-PBF processed Ti-6Al-4V spherical powder. They tested parts with different geometries to determine the effect of geometry on the fatigue behavior and their results from the geometry close to the samples fabricated in this study are shown in Figure 5. It was found that the fatigue performance of the specimens in this study was better than data reported by Pegues et al. [39]. This could be explained by the fact that samples were fabricated at an angle of 45° from the substrate [39], resulted in non-uniform surface roughness (rougher surface on the down-skin side compared to up-skin side). Gong et al. [41] showed that porosity volume of up to 1% would be harmless to the mechanical properties of the L-PBF processed Ti-6Al-4V spherical powder and their results were shown in Figure 5. The slightly better performance of those samples could be attributed to the lower surface roughness because of using finer powder compared to the used HDH powder in the present study. In another work by Benedetti et al. [40], very fine powder (mean size of 9 µm) was L-PBF processed followed by stress relief treatment at 670 °C for 5 h to investigate role of surface finish, defect, and mean stress sensitivity on the fatigue performance. Slightly better fatigue performance compared to the L-PBF processed HDH powder could be associated with lower surface roughness and the applied stress relief treatment leading to the minimal decomposition of martensite α' to an $\alpha+\beta$ structure with higher ductility. Soltani et al. [38] recently reported fatigue behavior of L-PBF processed Ti-6Al-4V using 34 µm spherical powder (see presented data in Figure 5). Similar microstructure of prior β grains containing acicular α' martensite lath was reported in [38], however, the slightly better fatigue performance compared to L-PBF processed HDH Ti-6Al-4V powder (with PSD of 50-120 µm) could be because of lower surface roughness from the use of spherical powder with much smaller particle size in the range 15-45 µm.

It should be noted that at higher stresses (*i.e.*, \geq 350 MPa) as shown in Figure 5, mechanically ground parts showed no significant improvement compared to the as-built samples. This can be explained by the fact that by removing the surface roughness, the inner defects (with potentially larger sizes) are effectively closer to the surface of the L-PBF HDH Ti-6Al-4V parts. As will be discussed in the fractography section, the subsurface defects were the main crack initiation sites in the mechanically ground parts. Moon et al. [50] used artificial intelligence to investigate the correlation between the surface roughness and fatigue life of the L-PBF processed Ti-6Al-4V parts. They fabricated parts using different processing parameters to study the effect of different porosity contents on fatigue performance. Porosities were divided into two groups of internal and surface

porosities separated by a depletion zone created by contour laser scanning. It was concluded that the fatigue life in as-built samples was primarily controlled by the microscale surface roughness of 7.7 µm which was evident through the positive correlation between the surface pore density and the fatigue life of the parts regardless of the stress amplitude. On the other hand, the correlation between the surface pore size and the fatigue life was more significant in the machined parts, thus, the number density of pores on the surface was not as important as their size. The same argument could be used to explain the negligible fatigue life improvement of the mechanically ground parts under high stress in the present study which was in agreement with the finding in Ref. [19]; the large defects were moved to the subsurface region after grinding the parts, thus, the mechanically ground parts failed more or less like the as-built parts under high stresses.

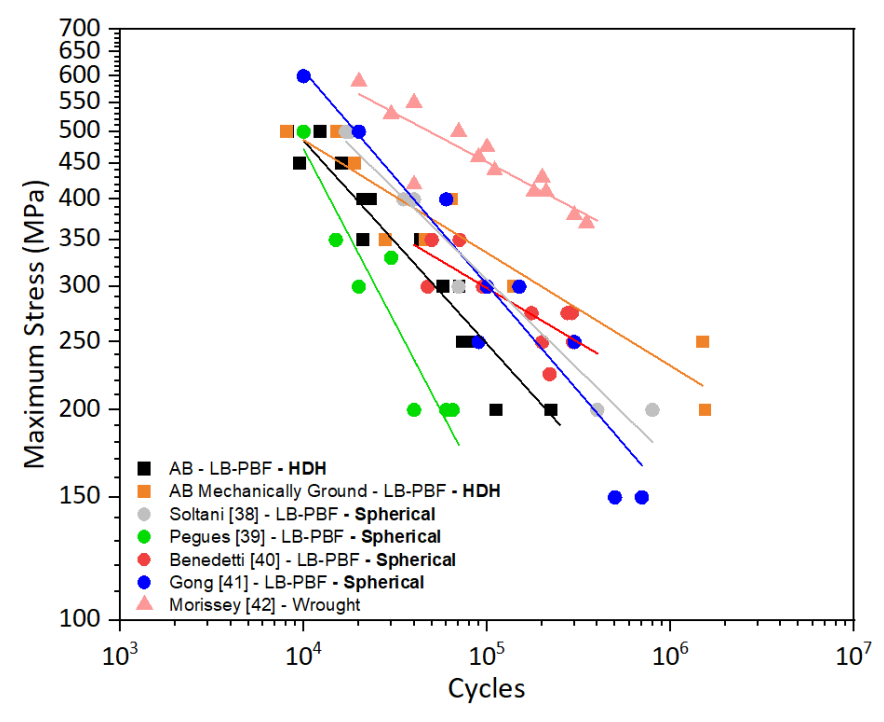


Figure 5. Fatigue life of L-PBF processed HDH Ti-6Al-4V powder in the as-built (black squares) and mechanically ground (orange squares) conditions compared with reference data of L-PBF processed spherical powder [38–41] and Ti-6Al-4V wrought alloy [42].

Micro-computed tomography (μ -CT) was done on one fatigue specimen before and after mechanically removing the surface roughness, Figure 6. The grinding process caused a 400 μ m reduction in the specimen diameter and 0.29 % reduction in porosity content from 0.35 % to 0.06 % before and after grinding, respectively. The argument mentioned above about the interior large defects being closer to the subsurface region because of machining is apparent in the μ -CT results. As it will be discussed in more detail in the fractography (section 3.4), the micro-notches on the surface of the as-built sample are the main stress concentrators, thus, the subsurface defects can be neglected. However, after removing the surface roughness, the micro-notches will be removed and the defects in the subsurface region are the main stress concentrators and crack initiation sites. The porosity analysis (see Figure 6e) showed removal of porosities larger than 80 μ m by the grinding surface. It can be concluded that the porosity distribution in the L-PBF processed HDH Ti-6Al-4V

samples is not uniform and relatively larger defects tend to form in the near surface region of the sample.

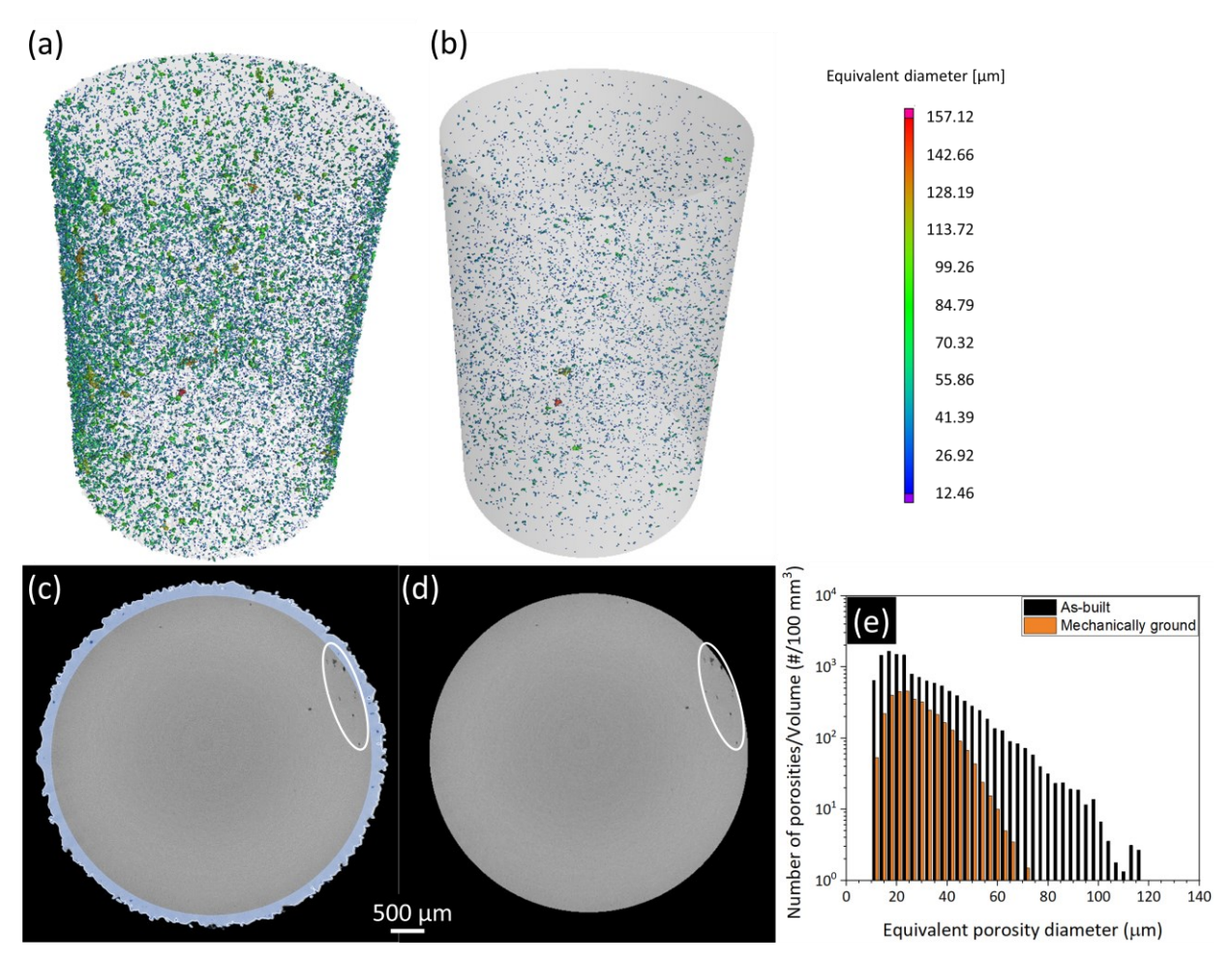


Figure 6. CT scan of a fatigue specimen in (a,c) as-built, and (b,d) mechanically ground conditions, and (e) normalized porosity count in 100 mm³ of gauge section of a fatigue specimen before and after mechanical grinding process. White ovals indicate the porosities that are moved from the (c) interior region to (d) subsurface region after grinding. Blue region in (a) shows the region that was removed from the fatigue specimen by mechanical grinding process.

The role of defect size on the fatigue performance of the parts was investigated using the average critical defect size analysis, Figure 7. The average critical size was measured using the formulation of Ref. [48]. The majority of the critical defects in the as-built sample were located on the surface of the sample and after grinding the sample, the critical defects were exclusively located in the subsurface and internal regions of the sample. This explains the fact that the crack initiation occurred exclusively from the surface defects in the as-built condition and from the subsurface defects in the mechanically ground samples.

Average critical size against the cycles to failure under the stress of 300 MPa was compared with the data from literature [40,51–53], Figure 7c. Our results agree with the data reported in the literature and shows decreasing fatigue life with increasing critical defect size in the samples, regardless of the location of the defects.

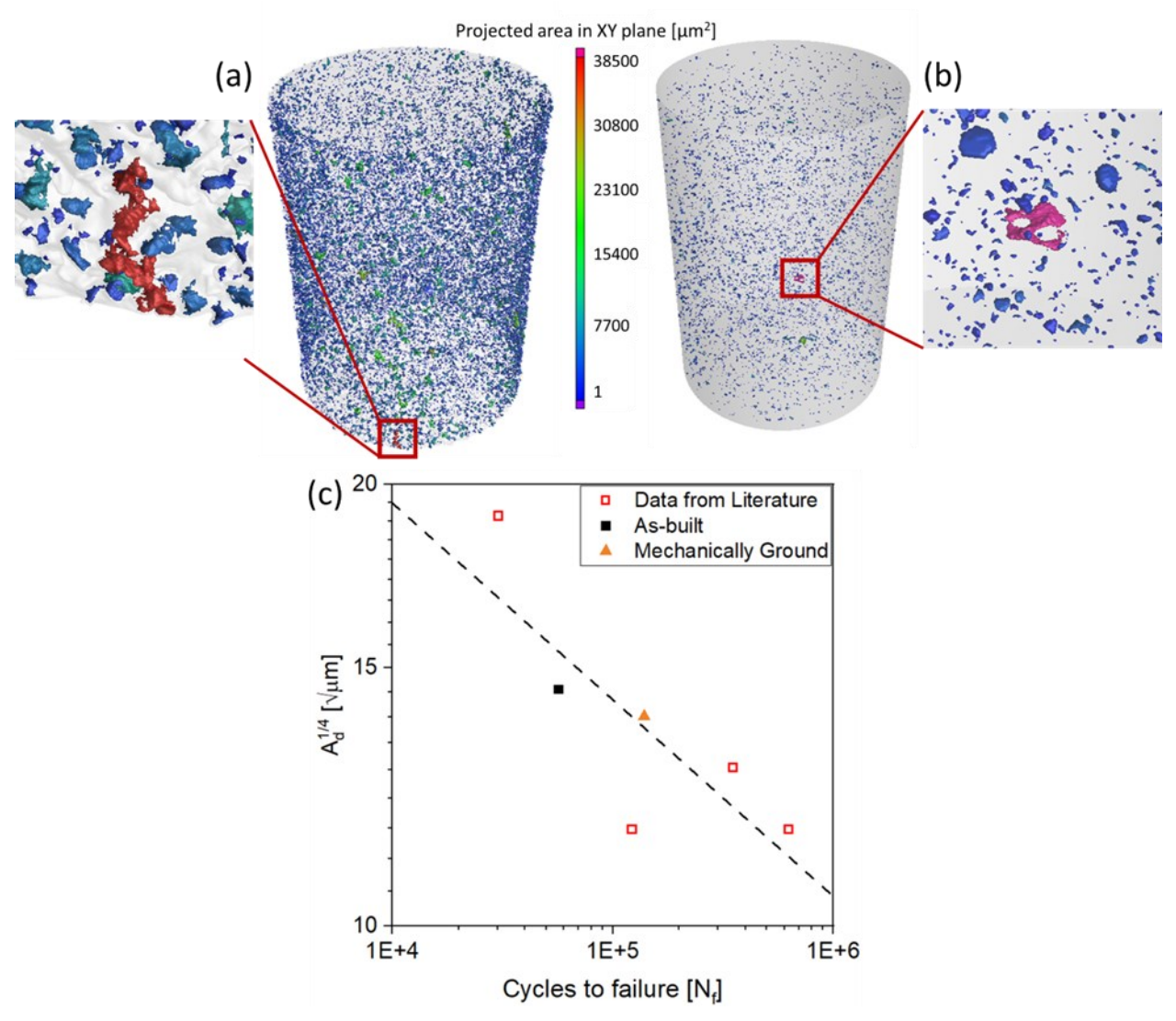


Figure 7. Defects with the largest projection area in the XY plane in the (a) as-built and (b) mechanically ground conditions, and (c) the average critical defect size against the cycles to failure under the stress of 300 MPa compared with the data from literature [40,51–53]. Note that the dashed line in (c) is the fitted line on the data with $R^2 = 0.72$, and the μ -CT was conducted on 10 mm height of the gauge section of the fatigue specimens.

3.3 Surface characterizations

3.3.1 Surface roughness assessment

Fatigue performance depends strongly on the surface condition; thus, it is crucial to quantify surface roughness. This was measured at eight different positions around the gauge area before and after mechanical grinding and the results are shown in Figure 8.

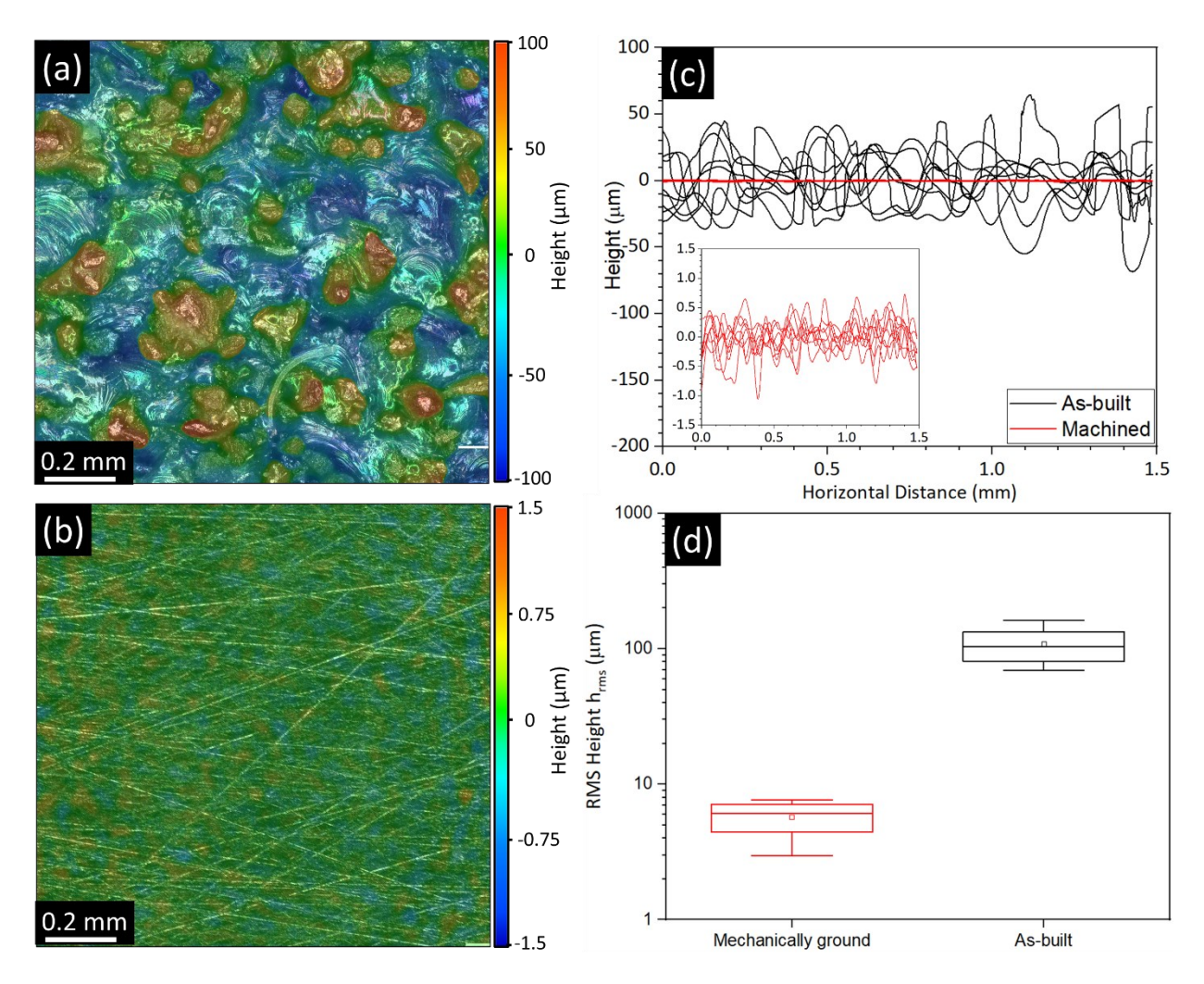


Figure 8. Optical surface topography profiles in (a) as-built and (b) mechanically ground conditions. (c) Line scans of surface topography of as-built and mechanically ground specimens obtained using optical profiler, and (d) comparison between h_{rms} values of different surface conditions.

The average roughness (R_a) and root-mean-squared height variation (h_{rms}) were calculated using the following equations on 2,160 points:

$$R_a = \frac{1}{n} \sum_{i=1}^{n} ABS(Z_i - Z_{mean})$$
 (Eq. 2)

$$h_{rms} = \sqrt{\frac{1}{n} \sum_{i=1}^{n} (Z_i)^2}$$
 (Eq. 3)

where n is number of points, Z_i is the height of each point in μ m, and Z_{mean} is the average height throughout the dataset in μ m. The R_a values for the samples before and after mechanical grinding were 15.71 ± 3.96 and 0.19 ± 0.04 μ m, respectively, i.e., a reduction by about two orders of magnitude. The h_{rms} value was reduced from 108.4 ± 24.9 (in an as-build condition) to 4.9 ± 0.6 μ m after the mechanical griding. This drastic change in surface roughness can explain better fatigue life of post surface treated L-PBF HDH Ti-6Al-4V specimens compared to the as-built surface condition, particularly under high cycle (low stress) conditions. Edwards et al. [18] used spherical powder with a mean size of 30 μ m and L-PBF and reported R_a and h_{rms} values in the

as-built condition of $38.5 \pm 2.3~\mu m$ and $47.4 \pm 2.4~\mu m$, respectively, while after machining, they were reduced to $0.89~\mu m$ and $1.2~\mu m$, respectively, i.e., a similar reduction. The higher h_{rms} value of L-PBF processed HDH Ti-6Al-4V specimens may be a consequence of the slightly larger layer thickness and much larger particle size used in this study. In another study on L-PBF of grade 23 ELI Ti-6Al-4V powder with a PSD of 10-45 μm , the R_a value was reported to be $17.2~\mu m$ [54]. This roughness was higher than the L-PBF processed components in the current study which could be related to sintering and partial melting of the powder particles sticking to the surface of the AM parts during the printing process.

A more quantitative approach is to relate the fatigue endurance limit of the as-built condition (σ_{e1}) to that of the mechanically ground specimen (σ_{e2}) by the effective fatigue notch factor (\overline{K}_f) , as expressed by the following equation [55]:

$$\sigma_{e1} = \frac{\sigma_{e2}}{\bar{K}_f} \tag{Eq. 4}$$

The fatigue notch factor (\overline{K}_f) can be calculated using the elastic stress concentration factor (\overline{K}_t) , and the notch sensitivity of the material (q) given by the following equations [55,56]:

$$\overline{K}_t = 1 + n(\frac{R_a}{\overline{\rho}_{10}})(\frac{R_t}{R_{ZISO}})$$
 (Eq. 5)

$$q = \frac{1}{1 + \frac{\gamma}{\overline{\rho}_{10}}} \tag{Eq. 6}$$

where n is a constant based on the changes in stress state (n=2 for tension), R_a is the average roughness, $\bar{\rho}_{10}$ is the average 10-point valley radii, R_t is the maximum peak-to-valley roughness, R_{zISO} is the 10-point height roughness, and γ is the average acicular α' lath width of the Ti-6Al-4V material, which is the average of α' lath widths of horizontal and vertical cross-sections in this study with the value of 1.05 μ m. R_a can be calculated using Eq. 2, and $\bar{\rho}_{10}$, R_t , and R_{zISO} can be calculated using the following equations [57]:

$$R_t = ABS(Z_{max} - Z_{min}) (Eq. 7)$$

$$R_{zISO} = \frac{1}{n} \left[\sum_{i=1}^{n} ABS(Z_i - Z_{max}) + \sum_{i=1}^{n} ABS(Z_i - Z_{min}) \right]$$
 (Eq. 8)

$$\bar{\rho}_{10} = \frac{1}{n} \sum_{i=1}^{n} \rho_{i-min}$$
 (Eq. 9)

where Z is the point height, Z_{max} is the maximum peak of the profile, Z_{min} is the minimum valley of the profile, and ρ_{i-min} are the radii of the deepest valleys. Figure 9 shows a line scan of surface roughness of the as-built specimen used to measure the deepest valleys' radii.

In (Eq. 5), \overline{K}_t shows a dependency on the $\frac{R_a}{\overline{\rho}_{10}}$ and $\frac{R_t}{R_{zISO}}$ ratios. With the sinusoidal basis of \overline{K}_t , one should be careful when taking these two ratios into account. The ratio $\frac{R_a}{\overline{\rho}_{10}}$ can describe the sinusoidal nature of \overline{K}_t when R_a is taken as the amplitude, and $\overline{\rho}_{10}$ is taken as the period of this waveform. Arola et al. [56] argued that the $\frac{R_t}{R_{zISO}}$ ratio would always be unity for an ideal sinusoidal surface, therefore, \overline{K}_t would only depend on the R_a and $\overline{\rho}_{10}$. These two parameters take the description of the depth and shape of the notches into account, so they are valid for estimation of the fatigue stress concentration because of the surface roughness. Table 4 lists the surface roughness parameters and stress concentration factors of the as-built samples. Pegues et al. [21]

reported mean notch radii and mean roughness of $23.77 \pm 11.06~\mu m$ and $22.65 \pm 5.41~\mu m$, respectively, for the samples fabricated using spherical powder. Also, they reported 4.42 as the calculated fatigue notch factor in their study. The measured mean roughness and mean notch radii in this study is significantly better. This difference can potentially result in better fatigue resistance by reducing the fatigue notch fatigue factor to 2.4. The significantly smaller fatigue notch factor of the parts manufactured with the HDH powder showed less dependence of the fatigue life on the surface roughness compared to the fine spherical powder. Now, if the fatigue notch factor and fatigue endurance limit of the mechanically ground specimens were assumed to be 1 (i.e., no notches on surface) and 250 MPa, respectively, the calculated fatigue endurance of the as-built sample would be 106.53 MPa (based on Eq. 4) which is reasonably close to the experimental value of 150 MPa in this study.

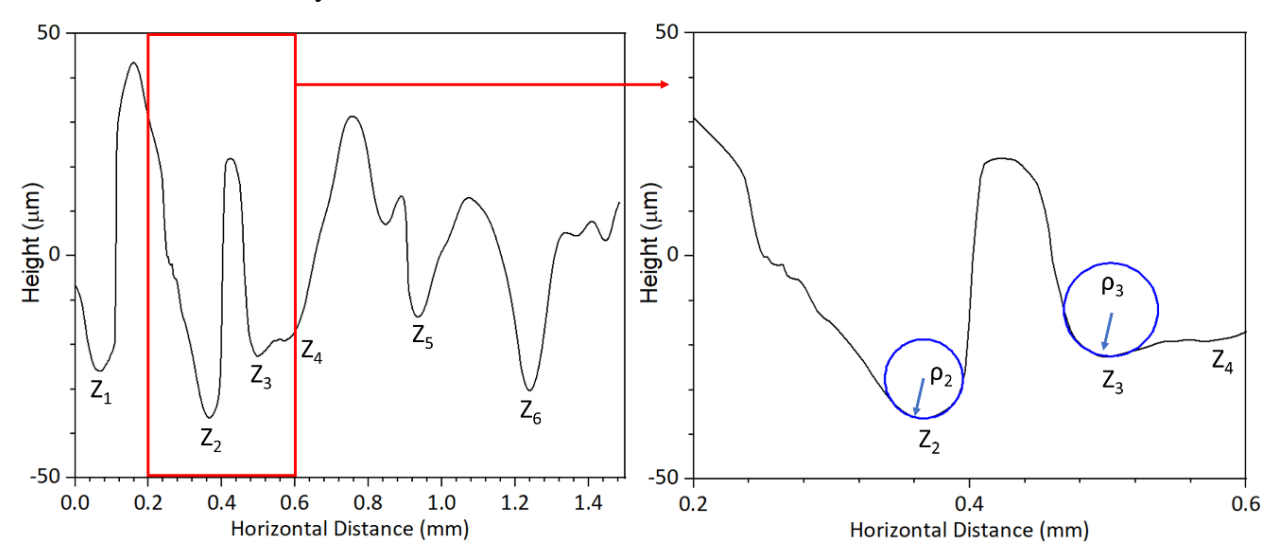


Figure 9. A line scan of surface roughness of the as-built specimen on the left, and two examples of the measurement of the deepest valleys radii on the right.

Table 4. Calculated surface roughness parameters and stress concentration factors of the as-built sample.

Parameter	R_a [µm]	R_t [μ m]	R_{zISO} [µm]	$ar{ ho}_{10}\left[\mu\mathrm{m} ight]$	q	\overline{K}_t	\overline{K}_f
Value	15.7 ± 4.0	83.3 ± 24.0	83.2 ± 24.0	22.2 ± 7.7	0.94	2.41	2.39

3.3.2 X-ray diffraction analysis

To further investigate the effect of surface grinding (and potentially surface stress) on the fatigue behavior of the L-PBF HDH Ti-6Al-4V parts, XRD was performed on both as-built and mechanically ground surfaces, Figure 10. Two main differences between the as-built and surface treated parts are (i) peak shifts and (ii) peak broadening after the post surface treatment. Quantitative analysis of the XRD patterns was performed using the MAUD software and the Rietveld refinement method [26]. For instance, on the (102) plane of the α' phase, there was a peak shift from 53.076° to 52.761° after mechanical grinding which resulted in elastic out-of-plane lattice expansion and in-plane compression indicated by increase in *d*-spacing of 1.724 to 1.733 Å

calculated by Bragg's law. Furthermore, micro-strain (ε) values for the as-built and mechanically ground samples were calculated using the following equation [58]:

$$\varepsilon = \frac{\beta}{4} \sin \theta \tag{Eq. 10}$$

where β is the full width at half maximum (FWHM) of the peak and θ is the Bragg angle of the (hkl) reflection. The calculated micro-strain was 0.0644 % in the as-built specimen and increased to 0.146 % after mechanical grinding, indicating compressive residual stress on the surface after surface polishing. This compressive residual stress could suppress the crack nucleation and enhance fatigue life.

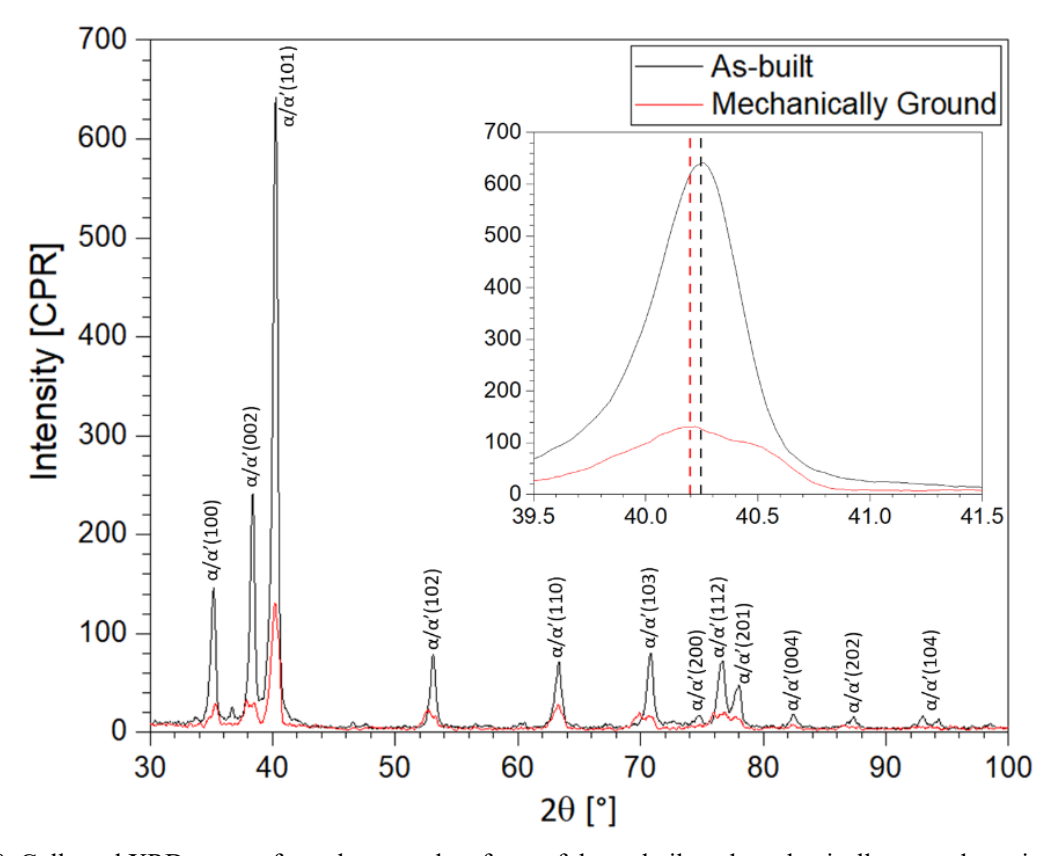


Figure 10. Collected XRD pattern from the curved surfaces of the as-built and mechanically ground specimens. The inset figure shows the peak shift at 40°, the black dashed line and the red dashed line indicate the peak center of as-built and mechanically ground conditions, respectively.

Table 5. Comparison of crystallographic parameters between as-built and mechanically ground samples from L-PBF processed HDH Ti-6Al-4V powder.

	A (101)			α (102)				α (110)				
	2θ	d-spacing	FWHM	ε	2θ	d-spacing	<i>FWHM</i>	ε	2θ	d-spacing	FWHM	3
	[°]	[Å]	[°]	[%]	[°]	[Å]	[°]	[%]	[°]	[Å]	[°]	[%]
As-built	40.216	2.24	0.50585	0.0462	53.076	1.724	0.516	0.0644	63.29	1.468	0.643	0.099
Mechanically ground	40.198	2.241	0.74935	0.0685	52.761	1.733	1.175	0.1456	63.239	1.469	0.978	0.1505

3.4 Fractography

Fractography was performed on all samples to investigate the potential differences in failure mechanisms between samples tested under different cyclic stresses. All as-built specimens had cracks originating from the surface of the samples, regardless of the cyclic stress. On the other hand, in the mechanically ground specimens, the cracks originated from internal defects, specifically, near surface defects. Figure 11a shows fatigue fracture surfaces of selected specimens tested under different stress amplitudes. As-built parts had multiple crack initiation sites compared to the mechanically ground condition with only one crack initiation site. Cracks in the as-built condition initiated on the surface from the high surface roughness, whereas mechanical grinding minimized surface roughness and the crack initiation sites were internal defects, specifically, pores near the surface (see Figure 11(b,c)). Moreover, the number of crack initiation sites and their spacing decreased with decreasing stress amplitude. In other words, as the stress amplitude increases, the number of stress concentration sites that pass the threshold condition increases, leading to earlier fatigue failure.

Figure 12(a,b) shows examples of different crack growth zones on the fatigue fracture surfaces of the as-built and mechanically ground samples that failed after 8,240 and 15,143 cycles, respectively, at a stress amplitude of 500 MPa. There were obvious differences between the crack growth zones. The as-built specimen showed two regions of early crack growth zone (green arrows) and a smaller third crack growth zone (white arrow) compared to the mechanically ground sample with only one first crack growth zone (green arrow) and a larger third crack growth zone (white arrow). Moreover, deterioration of the as-built sample's fracture surface was more obvious than the mechanically ground specimen. The tear ridges were more visible and the facets resulting from brittle fracture were larger in the as-built part compared to the mechanically ground sample.

To understand different stages of crack growth, SEM micrographs at higher magnification were collected and results are shown in Figure 12(c₁-c₃). Three different regions are seen in Figure 12(c₁) that could be defined as (1) region 1: unmelted particles sticking to the sample's surface, (2) region 2: partially melted particles during the contouring, and (3) region 3: stage one of crack nucleation and stable crack growth. Pegues *et al.* [39] reported that the presence of sharp micronotches between partially melted powders on the high roughness surface are potential crack initiation sites [46]. In Figure 12(c₁), several crack nucleation sites are indicated by blue arrows. Although each nucleation site resulted in crack propagation on a different plane, cracks coalesced in a single crack by the second stage of crack growth. These smaller cracks left behind a trace of distinct tear ridges as indicated by the red dashed line in Figure 12(c₁).

After coalescence of the small cracks, the big crack grows with a higher growth rate and less stability, thus, leaves behind some ductile fracture sites as indicated by the red color in Figure $12(c_2)$. The blue color region shows a portion of the sample after the second crack growth stage due to combination of cyclic and static failure modes that created a more tortuous crack path than the first crack growth stage [39]. The green arrow (see Figure $12(c_2)$) shows a secondary micro crack that could be an indicator of mixture of α' transgranular and prior β intergranular crack growth. As the crack grows during the second crack growth stage (quasi-stable crack growth), its stability decreases until the crack growth becomes sufficiently unstable to transform to the third crack growth stage (see Figure $12(c_2)$). The end of a β grain is visible and completely pulled out. This could be an indicator of the β intergranular failure and shows the shift from α' transgranular to β intergranular failure. At a large enough stress intensity (i.e., long enough crack), the fracture toughness limit is reached and sudden brittle failure occurs, leaving behind the shear lip at the edge of the sample (see region 4 in Figure 12(a,b)).

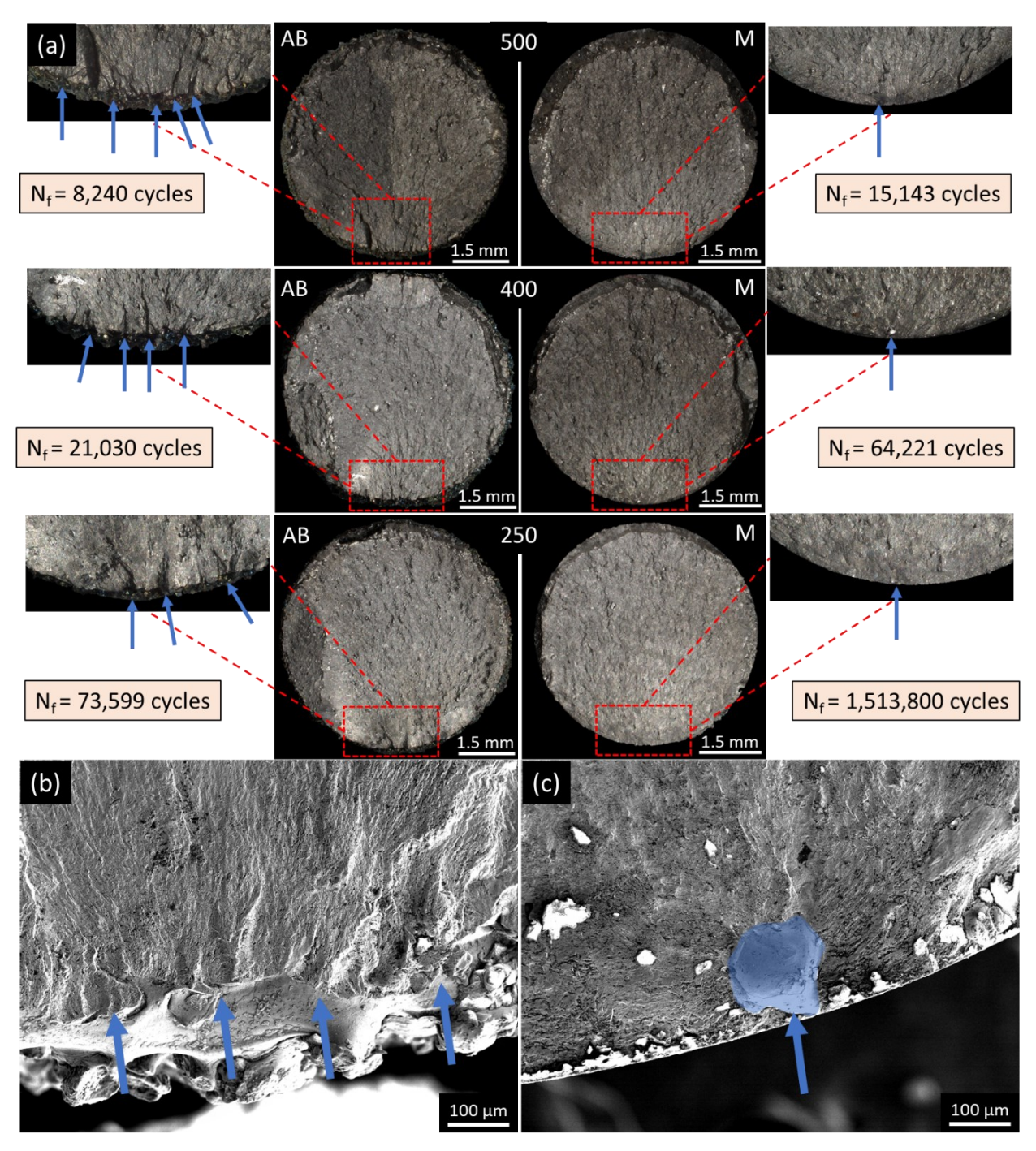


Figure 11. (a) Fatigue fracture surface of the L-PBF processed HDH Ti-6Al-4V powder tested under different stress amplitudes. Blue arrows indicate crack initiation sites. "AB" represents as-built parts and "M" represents mechanically ground parts. SEM micrographs of samples tested under stress amplitude of 500 MPa showing crack initiation sites for the (b) as-built and (c) mechanically ground conditions.

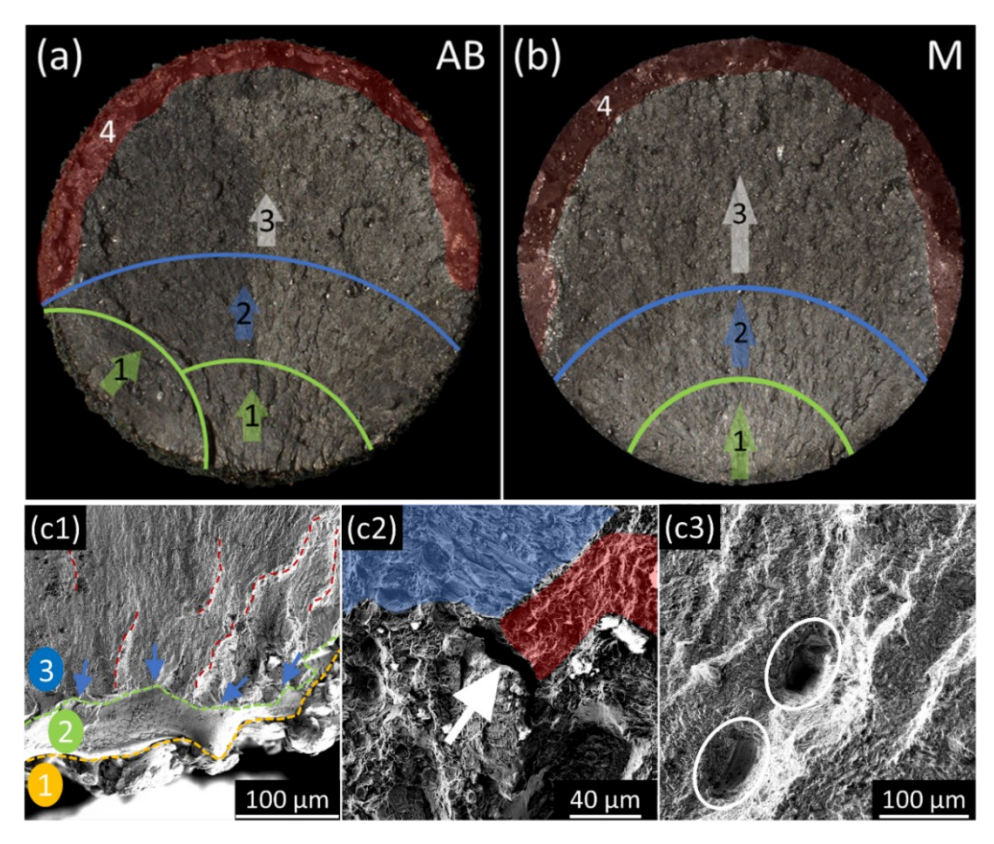


Figure 12. Different crack growth stages shown on the (a) as-built and (b) mechanically ground samples tested under stress amplitude of 500 MPa. Numbers represent different crack growth zones including the crack nucleation and stable crack growth stage (1, green arrow), a quasi-stable crack growth stage (2, blue arrow), and unstable crack growth stage (3, white arrow). At the end, after final stage of crack propagation, the stress concentration increases due to the surface area reduction and the final fracture occurs (4, red region). SEM micrographs indicating (c_1) first stage, (c_2) second stage, and (c_3) third stage of crack growth. Blue arrows and red lines in (c_1) show crack nucleation sites and tear ridges, respectively. Numbers 1, 2, and 3 in (c_1) show unmelted powders, partially melted particles during the contouring, and crack growth zone, respectively. Blue and red regions in (c_2) show stable crack growth striations and ductile tearing, respectively. White arrow in (c_2) shows a microcrack. White ovals in (c_3) show the trace of β grains that were pulled out.

Figure 13 shows the gradual change of fracture modes from pseudo-brittle to ductile when moving from the second to third crack growth regions in the fatigue failure (as explained in Figure 12(a,b)). The main difference between the second and third crack growth zones is the cross-sectional area that is under cyclic stress, i.e., the increased stress intensity. As the crack grows, the remaining cross-sectional area of the part decreases with corresponding increase in stress intensity, resulting in change of fracture mode. The rising local stress results in higher rate of local deformation in martensitic features, and consequently, higher dominance of ductile fracture features compared to the brittle features. Moridi et al. [59] investigated the local deformation mechanism in L-PBF processed Ti-6AL-4V parts and concluded that local void formation occurs inside the primary α' at a 45° orientation with respect to the loading axis owing to the high Schmid factor. Thus, growth and coalescence of voids resulted in final fracture. Interestingly, this local damage is highly ductile, but the final fracture is brittle. The combination of ductile dimple and brittle cleavage features on fracture surfaces (see Figure 13) in the present study is consistent with the findings of Moridi et al. [59] and confirmed the pseudo-embrittlement phenomenon.

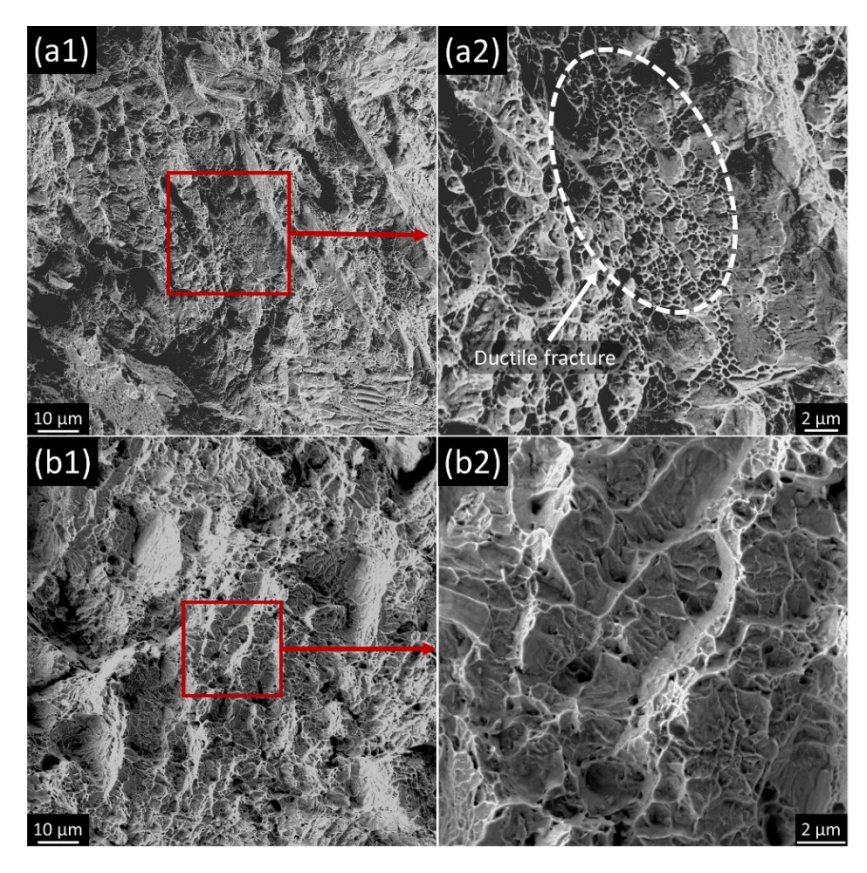


Figure 13. SEM micrographs of the fatigue fracture surface of the L-PBF processed HDH Ti-6Al-4V part tested under stress amplitude of 500 MPa. (a_1,a_2) showing the brittle fracture surface containing small ductile fracture features from the second crack growth zone, and (b_1,b_2) showing the dominant ductile fracture surface and brittle cleavage features in the third crack growth zone.

Figure 14 shows optical images from the side and top surface of the as-built condition indicating the micro-notches, partially melted powder particles, laser path, and contouring effect on the surface morphology of the parts. Contouring after scanning the hatch area was used in this study to mitigate the effect of laser scanning near the surface on the surface roughness. However, near surface and on surface defects can be introduced based on the parameters used for contouring. For example, Artzt el al. [60] reported that increasing the laser power used for contouring resulted in higher surface roughness and lower subsurface residual stress in L-PBF Ti-6Al-4V. In the present study, contouring resulted in elevation of the free edge of the parts (see Figure 14d) which could disrupt the powder spreading uniformity and caused different kinds of defects in the parts, especially, near the edges. As mentioned earlier, defects on surface (e.g., micro-notches) and subsurface (e.g., near surface pores) areas are the main crack initiation sites (see Figure 11(b,c)).

Micro-notches occur between two or more adjacent powder particles, either in the same layer or between consecutive layers, and act as stress concentrators, i.e., potential crack initiator sites. Wycisk et al. [61] reported that the as-built L-PBF processed Ti-6Al-4V samples fail only through surface defects, i.e. surface micro-notches. Furthermore, they argued that the fatigue life is strongly dependent on the crack initiation stage. Edwards et al. [62] investigated the effect of build direction on fatigue crack growth of the L-PBF processed Ti-6Al-4V parts. They tested samples under R = 0.1 condition and reported that the crack growth is slower in AM parts compared to the wrought alloy. Vayssette et al. [63]tested three different sets of L-PBF processed Ti-6Al-4V parts in the as-

built, machined, and chemically polished conditions under R = -1 and concluded that chemically polishing the parts does not improve the fatigue life compared to the as-built condition despite the reduction of surface roughness from 18.9 µm (in as-build) to 11.2 µm (in the chemically polished condition). They also reported that chemically polishing only eliminates the powder grains on the surface and reduces the R_a value, however, the large defects are still present. Moreover, chemically polishing may bring up new type of defects which influence was not apparent in the as-built condition because of large number of smaller but more critical defects. Therefore, the fatigue crack initiation occurred exclusively from the defects on the surface in the as-built and chemically polished samples. On the other hand, they showed that machining process increases the fatigue strength of the L-PBF parts because it removes the surface roughness. Chan et al. [64] showed that the decrease in surface roughness of L-PBF processed Ti-6Al-4V parts led to higher fatigue life. They were able to increase the mean fatigue life of parts by 17,000 cycles after decreasing the surface roughness from 38.5 to 7.67 µm. Moreover, they reported that the cracks initiated from the micro-notches between the partially melted particles on the surface of the additively manufactured parts. Masuo et al. [53] investigated the effect of surface roughness on fatigue life of L-PBF Ti-6Al-4V parts and showed that the fatigue limit was increased by 215 MPa after comparing the fatigue test results of as-built parts (with a fatigue limit of 155 MPa) with surface roughness of order 10-13 µm and machined parts (with a fatigue limit of 370 MPa).

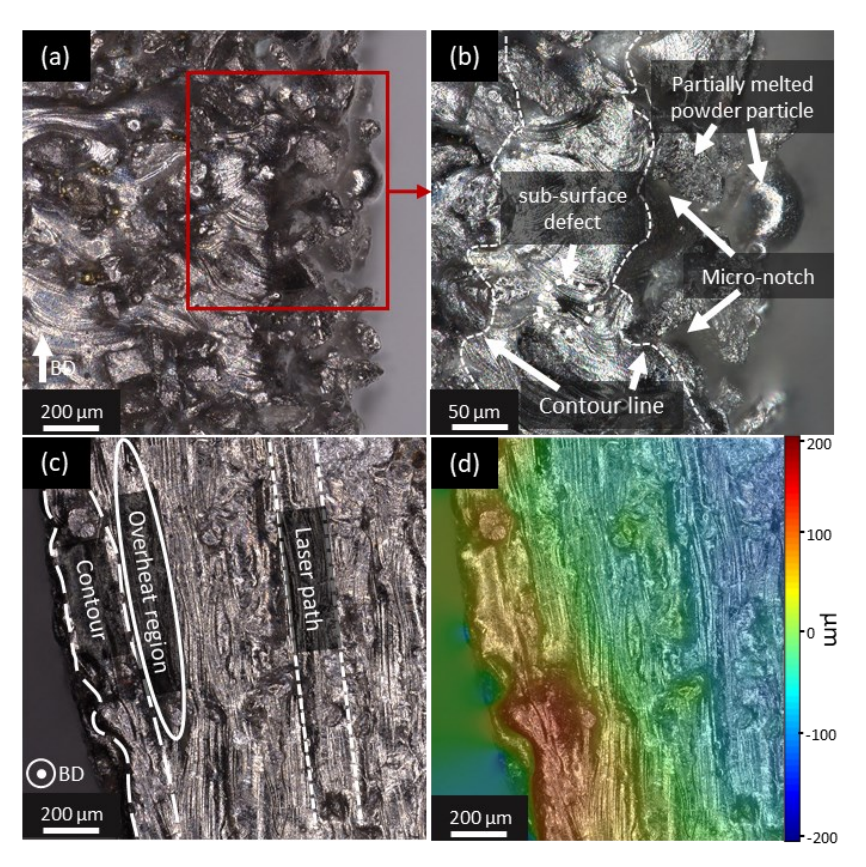


Figure 14. Optical images of the (a,b) side and (c,d) top surfaces of L-PBF processed HDH Ti-6Al-4V parts. (d) the corresponding surface topography of (c).

4. Conclusion

In this study, non-spherical HDH Ti-6Al-4V powder were used to study the effects of powder particle shape on the fatigue performance of the L-PBF parts. Specimens were tested under R = -1 in two conditions of as-built and mechanically ground to assess the surface roughness dependency of fatigue properties. Below are the conclusions drawn from the results:

- The fatigue performance of the parts fabricated using non-spherical powder was comparable to that of the spherical ones for an equivalent surface condition. The reduction of surface roughness from 15.71 ± 3.96 in the as-built sample to 0.19 ± 0.04 μm in the mechanically ground condition lowered the stress concentrators on the surface, i.e., potential crack initiation sites, thus, improved fatigue life in the low stress region. However, under high stresses, the mechanically ground parts showed negligible improvement in fatigue life compared to the asbuilt specimens because grinding exposed previously inner defects on the subsurface region and created critical crack initiation sites. In fact, the fatigue life was also greatly affected by the residual compressive stress and surface roughness in the low stress region, however, under high stresses, the fatigue life was controlled by the size and density of the internal or surface defects.
- Fatigue notch factor calculations showed a value of 2.4 for the as-built sample compared to 4.42 reported in [21] for spherical powder which suggests that the effect of surface roughness is lower when HDH powder is used compared to the spherical powder. X-ray analysis showed an in-plane compressive residual stress and grain refinement on the surface of the mechanically ground specimens which enhanced fatigue life by suppression of the crack initiations sites.
- In the as-built specimens, cracks initiated exclusively from multiple points on the surface owing to the micro-notches between the adjacent partially melted powder particles on the surface, whereas the crack initiation site changed to a single subsurface defect after mechanical grinding. Different fracture surfaces were observed on the tested specimens in which the first stage of crack growth was fully brittle fracture, the second stage showed mixed ductile and brittle fracture, and finally the third stage was mainly dominated by ductile fracture. On the other hand, at the micro scale, even apparently brittle fracture had a ductile origin inside α' martensite laths which corresponded to the pseudo-embrittlement phenomenon.

This study showed that cost-effective non-spherical powders are viable feedstocks for the L-PBF process in which as-fabricated parts with a relative density of > 99.9 % are attained. Further studies such as varying the contouring parameters to reduce surface roughness, role of post-heat treatment on final density and microstructure, and establishing a process-structure-property relationship are suggested to advance the application of the HDH powder in powder bed AM.

Acknowledgements

AM acknowledges startup funding from Mechanical, Materials and Aerospace Engineering Department at Illinois Institute of Technology at Chicago, Illinois. Authors acknowledge partial support from the National Science Foundation under grant number DMR-2050916. Also, this work is supported in part by the Pennsylvania Infrastructure Technology Alliance, a partnership of Carnegie Mellon, Lehigh University and the Commonwealth of Pennsylvania's Department of Community and Economic Development (DCED). The authors recognize Reading Alloys (formerly affiliated with AMETEK Inc., now a part of Kymera International), especially Mike Marucci, for providing the Ti-6Al-4V powder used in this work, and assistance with the study. Authors also acknowledge Abhilash Dinkar, Krishna Sai Vishnumolakala, and Melody H.

Delpazir for the assistance during sample preparation. ZW was supported under the auspices of the U.S. Department of Energy by Lawrence Livermore National Laboratory under contract DE-AC52-07NA27344. Release LLNL-JRNL-836489. IM release number LLNL-JRNL-834850.

References

- [1] V. Duz, A. Klevtsov, V. Sukhoplyuyev, Production of titanium powder, ASM International, 2015. https://doi.org/10.31399/asm.hb.v07.9781627081757.
- [2] G. Chen, S.Y. Zhao, P. Tan, J. Wang, C.S. Xiang, H.P. Tang, A comparative study of Ti-6Al-4V powders for additive manufacturing by gas atomization, plasma rotating electrode process and plasma atomization, Powder Technol. 333 (2018) 38–46. https://doi.org/10.1016/j.powtec.2018.04.013.
- [3] N.R. Philips, M. Carl, N.J. Cunningham, New Opportunities in Refractory Alloys, Metall. Mater. Trans. A Phys. Metall. Mater. Sci. 51 (2020) 3299–3310. https://doi.org/10.1007/s11661-020-05803-3.
- [4] G.S. Altug-Peduk, S. Dilibal, O. Harrysson, S. Ozbek, H. West, Characterization of Ni–Ti Alloy Powders for Use in Additive Manufacturing, Russ. J. Non-Ferrous Met. 59 (2018) 433–439. https://doi.org/10.3103/S106782121804003X.
- [5] A. Mostafaei, P. Rodriguez De Vecchis, E.L. Stevens, M. Chmielus, Sintering regimes and resulting microstructure and properties of binder jet 3D printed Ni-Mn-Ga magnetic shape memory alloys, Acta Mater. 154 (2018) 355–364. https://doi.org/https://doi.org/10.1016/j.actamat.2018.05.047.
- [6] R. Cunningham, A. Nicolas, J. Madsen, E. Fodran, E. Anagnostou, M.D. Sangid, A.D. Rollett, Analyzing the effects of powder and post-processing on porosity and properties of electron beam melted Ti-6Al-4V, Mater. Res. Lett. 5 (2017) 516–525. https://doi.org/10.1080/21663831.2017.1340911.
- [7] S. Li, H. Hassanin, M.M. Attallah, N.J.E. Adkins, K. Essa, The development of TiNi-based negative Poisson's ratio structure using selective laser melting, Acta Mater. 105 (2016) 75–83. https://doi.org/https://doi.org/10.1016/j.actamat.2015.12.017.
- [8] A.J. Brooks, J. Ge, M.M. Kirka, R.R. Dehoff, H.Z. Bilheux, N. Kardjilov, I. Manke, L.G. Butler, Porosity detection in electron beam-melted Ti-6Al-4V using high-resolution neutron imaging and grating-based interferometry, Prog. Addit. Manuf. 2 (2017) 125–132. https://doi.org/10.1007/s40964-017-0025-z.
- [9] S. Tammas-Williams, P.J. Withers, I. Todd, P.B. Prangnell, Porosity regrowth during heat treatment of hot isostatically pressed additively manufactured titanium components, Scr. Mater. 122 (2016) 72–76. https://doi.org/10.1016/j.scriptamat.2016.05.002.
- [10] D.P. Barbis, R.M. Gasior, G.P. Walker, J.A. Capone, T.S. Schaeffer, Titanium powders from the hydride-dehydride process, in: Titan. Powder Metall. Sci. Technol. Appl., Elsevier Inc., 2015: pp. 101–116. https://doi.org/10.1016/B978-0-12-800054-0.00007-1.
- [11] D. Basu, Z. Wu, J.L.L. Meyer, E. Larson, R. Kuo, A. Rollett, Entrapped Gas and Process Parameter-Induced Porosity Formation in Additively Manufactured 17-4 PH Stainless Steel, J. Mater. Eng. Perform. 30 (2021) 5195–5202. https://doi.org/10.1007/s11665-021-05695-3.
- [12] M. Asherloo, Z. Wu, E. Ghebreiesus, S. Fryzlewicz, R. Jiang, B. Gould, M. Heim, D. Nelson, M. Marucci, M. Paliwal, A.D. Rollett, A. Mostafaei, Laser-beam powder bed fusion of cost-effective non-spherical hydride-dehydride Ti-6Al-4V alloy, Curr. Opin. Solid State Mater. Sci. 56 (2022) 102875.

- [13] S.P. Narra, Z. Wu, R. Patel, J. Capone, M. Paliwal, J. Beuth, A. Rollett, Use of Non-Spherical Hydride-Dehydride (HDH) Powder in Powder Bed Fusion Additive Manufacturing, Addit. Manuf. 34 (2020) 101188. https://doi.org/10.1016/j.addma.2020.101188.
- [14] Z. Wu, M. Asherloo, R. Jiang, M.H. Delpazir, N. Sivakumar, M. Paliwal, J. Capone, B. Gould, A. Rollett, A. Mostafaei, Study of Printability and Porosity Formation in Laser Powder Bed Fusion Built Hydride-Dehydride (HDH) Ti-6Al-4V, Addit. Manuf. 47 (2021) 102323.
- [15] F. Medina, Reducing metal alloy powder costs for use in powder bed fusion additive manufacturing: Improving the economics for production, The University of Texas at El Paso, 2013.
- [16] H. Jaber, T. Kovacs, K. János, Investigating the impact of a selective laser melting process on Ti6Al4V alloy hybrid powders with spherical and irregular shapes, Adv. Mater. Process. Technol. (2020) 1–17. https://doi.org/10.1080/2374068X.2020.1829960.
- [17] J. Varela, E. Arrieta, M. Paliwal, M. Marucci, J.H. Sandoval, J.A. Gonzalez, B. McWilliams, L.E. Murr, R.B. Wicker, F. Medina, Investigation of Microstructure and Mechanical Properties for Ti-6Al-4V Alloy Parts Produced Using Non-Spherical Precursor Powder by Laser Powder Bed Fusion, Materials (Basel). 14 (2021) 3028. https://doi.org/10.3390/ma14113028.
- [18] P. Edwards, M. Ramulu, Fatigue performance evaluation of selective laser melted Ti-6Al-4V, Mater. Sci. Eng. A. 598 (2014) 327–337.
- [19] H. Gong, K. Rafi, T. Starr, B. Stucker, Effect of Defects on Fatigue Tests of As-Build Ti-6Al-4V Parts Fabricated by Selective Laser Melting, in: Int. Solid Free. Fabr. Symp., 2012. https://doi.org/dx.doi.org/10.26153/tsw/15369.
- [20] V. Cain, L. Thijs, J. Van Humbeeck, B. Van Hooreweder, R. Knutsen, Crack propagation and fracture toughness of Ti6Al4V alloy produced by selective laser melting, Addit. Manuf. 5 (2015) 68–76. https://doi.org/10.1016/j.addma.2014.12.006.
- [21] J.W. Pegues, N. Shamsaei, M.D. Roach, R.S. Williamson, Fatigue life estimation of additive manufactured parts in the as-built surface condition, Mater. Des. Process. Commun. 1 (2019) e36. https://doi.org/10.1002/mdp2.36.
- [22] A. Mostafaei, C. Zhao, Y. He, S. Reza Ghiaasiaan, B. Shi, S. Shao, N. Shamsaei, Z. Wu, N. Kouraytem, T. Sun, J. Pauza, J. V. Gordon, B. Webler, N.D. Parab, M. Asherloo, Q. Guo, L. Chen, A.D. Rollett, Defects and anomalies in powder bed fusion metal additive manufacturing, Curr. Opin. Solid State Mater. Sci. 26 (2022) 100974. https://doi.org/10.1016/j.cossms.2021.100974.
- [23] ASTM B348: Standard Specification for Titanium and Titanium Alloy Bars and Billets, Vol 02.04, (n.d.).
- [24] F. Bachmann, R. Hielscher, H. Schaeben, Texture Analysis with MTEX Free and Open Source Software Toolbox, Solid State Phenom. 160 (2010) 63–68. https://doi.org/10.4028/www.scientific.net/SSP.160.63.
- [25] S. Gates-Rector, T. Blanton, The Powder Diffraction File: a quality materials characterization database, Powder Diffr. 34 (2019) 1–9. https://doi.org/10.1017/S0885715619000812.
- [26] L. Lutterotti, Total pattern fitting for the combined size–strain–stress–texture determination in thin film diffraction, Nucl. Instruments Methods Phys. Res. Sect. B Beam Interact. with Mater. Atoms. 268 (2010) 334–340.

- https://doi.org/https://doi.org/10.1016/j.nimb.2009.09.053.
- [27] S. Liu, Y.C. Shin, Additive manufacturing of Ti6Al4V alloy: A review, Mater. Des. 164 (2019) 107552. https://doi.org/10.1016/j.matdes.2018.107552.
- [28] S.A. Oh, R.E. Lim, J.W. Aroh, A.C. Chuang, B.J. Gould, B. Amin-Ahmadi, J. V. Bernier, T. Sun, P.C. Pistorius, R.M. Suter, A. D.Rollett, High speed synchrotron X-ray diffraction experiments resolve microstructure and phase transformation in laser processed Ti-6Al-4V, Mater. Res. Lett. 9 (2021) 429–436. https://doi.org/10.1080/21663831.2021.1966537.
- [29] E. Fereiduni, A. Ghasemi, M. Elbestawi, Microstructural characterization and mechanical properties of nano-scale/sub-micron TiB-reinforced titanium matrix composites fabricated by laser powder bed fusion, J. Alloys Compd. 896 (2022) 163054. https://doi.org/https://doi.org/10.1016/j.jallcom.2021.163054.
- [30] P.A. Kobryn, S.L. Semiatin, Microstructure and texture evolution during solidification processing of Ti-6A1-4V, J. Mater. Process. Technol. 135 (2003) 330–339. https://doi.org/10.1016/S0924-0136(02)00865-8.
- [31] L. Thijs, F. Verhaeghe, T. Craeghs, J. Van Humbeeck, J.P. Kruth, A study of the microstructural evolution during selective laser melting of Ti-6Al-4V, Acta Mater. 58 (2010) 3303–3312. https://doi.org/10.1016/j.actamat.2010.02.004.
- [32] F. Niessen, T. Nyyssönen, A.A. Gazder, R. Hielscher, Parent grain reconstruction from partially or fully transformed microstructures in {\it MTEX}, J. Appl. Crystallogr. 55 (2022) 180–194. https://doi.org/10.1107/S1600576721011560.
- [33] J.G. Pauza, W.A. Tayon, A.D. Rollett, Computer simulation of microstructure development in powder-bed additive manufacturing with crystallographic texture, Model. Simul. Mater. Sci. Eng. 29 (2021) 55019. https://doi.org/10.1088/1361-651x/ac03a6.
- [34] J.M. Vitek, The effect of welding conditions on stray grain formation in single crystal welds

 theoretical analysis, Acta Mater. 53 (2005) 53–67. https://doi.org/https://doi.org/10.1016/j.actamat.2004.08.039.
- [35] Z. Wang, Z. Xiao, Y. Tse, C. Huang, W. Zhang, Optimization of processing parameters and establishment of a relationship between microstructure and mechanical properties of SLM titanium alloy, Opt. Laser Technol. 112 (2019) 159–167. https://doi.org/10.1016/j.optlastec.2018.11.014.
- [36] E. Fereiduni, A. Ghasemi, M. Elbestawi, Unique opportunities for microstructure engineering via trace B4C addition to Ti-6Al-4V through laser powder bed fusion process: As-built and heat-treated scenarios, Addit. Manuf. 50 (2022) 102557. https://doi.org/https://doi.org/10.1016/j.addma.2021.102557.
- [37] T. Voisin, N.P. Calta, S.A. Khairallah, J.B. Forien, L. Balogh, R.W. Cunningham, A.D. Rollett, Y.M. Wang, Defects-dictated tensile properties of selective laser melted Ti-6Al-4V, Mater. Des. 158 (2018) 113–126. https://doi.org/10.1016/j.matdes.2018.08.004.
- [38] A. Soltani-Tehrani, M. Habibnejad-Korayem, S. Shao, M. Haghshenas, N. Shamsaei, Ti-6Al-4V powder characteristics in laser powder bed fusion: The effect on tensile and fatigue behavior, Addit. Manuf. 51 (2022) 102584. https://doi.org/https://doi.org/10.1016/j.addma.2021.102584.
- [39] J. Pegues, M. Roach, R. Scott Williamson, N. Shamsaei, Surface roughness effects on the fatigue strength of additively manufactured Ti-6Al-4V, Int. J. Fatigue. 116 (2018) 543–552. https://doi.org/10.1016/j.ijfatigue.2018.07.013.
- [40] M. Benedetti, V. Fontanari, M. Bandini, F. Zanini, S. Carmignato, Low- and high-cycle fatigue resistance of Ti-6Al-4V ELI additively manufactured via selective laser melting:

- Mean stress and defect sensitivity, Int. J. Fatigue. 107 (2018) 96–109. https://doi.org/10.1016/j.ijfatigue.2017.10.021.
- [41] H. Gong, K. Rafi, H. Gu, G.D. Janaki Ram, T. Starr, B. Stucker, Influence of defects on mechanical properties of Ti-6Al-4V components produced by selective laser melting and electron beam melting, Mater. Des. 86 (2015) 545–554. https://doi.org/10.1016/j.matdes.2015.07.147.
- [42] R.J. Morrissey, T. Nicholas, Fatigue strength of Ti–6Al–4V at very long lives, Int. J. Fatigue. 27 (2005) 1608–1612. https://doi.org/10.1016/j.ijfatigue.2005.07.009.
- [43] F.C. Campbell, Fatigue and fracture: understanding the basics, ASM International, 2012.
- [44] A. Mostafaei, S.H.V.R. Neelapu, C. Kisailus, L.M. Nath, T.D.B. Jacobs, M. Chmielus, Characterizing surface finish and fatigue behavior in binder-jet 3D-printed nickel-based superalloy 625 Characterizing surface finish and fatigue behavior in binder-jet 3D-printed nickel-based superalloy 625, Addit. Manuf. 24 (2018) 200–209.
- [45] A.S.M.H. Committee, Fatigue and Fracture, (1996). https://doi.org/10.31399/asm.hb.v19.9781627081931.
- [46] C.A. Kantzos, R.W. Cunningham, V. Tari, A.D. Rollett, Characterization of metal additive manufacturing surfaces using synchrotron X-ray CT and micromechanical modeling, Comput. Mech. 61 (2018) 575–580. https://doi.org/10.1007/s00466-017-1531-z.
- [47] C.-W. Lin, C.-P. Ju, J.-H. Chern Lin, A comparison of the fatigue behavior of cast Ti-7.5Mo with c.p. titanium, Ti-6Al-4V and Ti-13Nb-13Zr alloys, Biomaterials. 26 (2005) 2899–2907. https://doi.org/https://doi.org/10.1016/j.biomaterials.2004.09.007.
- [48] N. Sanaei, A. Fatemi, Analysis of the effect of internal defects on fatigue performance of additive manufactured metals, Mater. Sci. Eng. A. 785 (2020) 139385. https://doi.org/https://doi.org/10.1016/j.msea.2020.139385.
- [49] B.L. Boyce, R.O. Ritchie, Effect of load ratio and maximum stress intensity on the fatigue threshold in Ti–6Al–4V, Eng. Fract. Mech. 68 (2001) 129–147. https://doi.org/https://doi.org/10.1016/S0013-7944(00)00099-0.
- [50] S. Moon, R. Ma, R. Attardo, C. Tomonto, M. Nordin, P. Wheelock, M. Glavicic, M. Layman, R. Billo, T. Luo, Impact of surface and pore characteristics on fatigue life of laser powder bed fusion Ti–6Al–4V alloy described by neural network models, Sci. Rep. 11 (2021) 20424. https://doi.org/10.1038/s41598-021-99959-6.
- [51] J. Günther, D. Krewerth, T. Lippmann, S. Leuders, T. Tröster, A. Weidner, H. Biermann, T. Niendorf, Fatigue life of additively manufactured Ti–6Al–4V in the very high cycle fatigue regime, Int. J. Fatigue. 94 (2017) 236–245. https://doi.org/10.1016/j.ijfatigue.2016.05.018.
- [52] A.J. Sterling, B. Torries, N. Shamsaei, S.M. Thompson, D.W. Seely, Fatigue behavior and failure mechanisms of direct laser deposited Ti-6Al-4V, Mater. Sci. Eng. A. 655 (2016) 100–112. https://doi.org/10.1016/j.msea.2015.12.026.
- [53] H. Masuo, Y. Tanaka, S. Morokoshi, H. Yagura, T. Uchida, Y. Yamamoto, Y. Murakami, Influence of defects, surface roughness and HIP on the fatigue strength of Ti-6Al-4V manufactured by additive manufacturing, Int. J. Fatigue. 117 (2018) 163–179. https://doi.org/10.1016/j.ijfatigue.2018.07.020.
- [54] M.A. Obeidi, A. Mussatto, M.N. Dogu, S.P. Sreenilayam, E. McCarthy, I.U. Ahad, S. Keaveney, D. Brabazon, Laser surface polishing of Ti-6Al-4V parts manufactured by laser powder bed fusion, Surf. Coatings Technol. 434 (2022) 128179. https://doi.org/10.1016/j.surfcoat.2022.128179.

- [55] H. Neuber, Theory of notch stresses: principles for exact calculation of strength with reference to structural form and material, USAEC Office of Technical Information, 1961.
- [56] D. Arola, M. Ramulu, An examination of the effects from surface texture on the strength of fiber reinforced plastics, J. Compos. Mater. 33 (1999) 102–123.
- [57] ASTM B946-06 Standard Test Method for Surface Finish of Powder Metallurgy (P/M) Products, (2006).
- [58] S. Dai, Y. Zhu, Z. Huang, Microstructure evolution and strengthening mechanisms of pure titanium with nano-structured surface obtained by high energy shot peening, Vacuum. 125 (2016) 215–221.
- [59] A. Moridi, A.G. Demir, L. Caprio, A.J. Hart, B. Previtali, B.M. Colosimo, Deformation and failure mechanisms of Ti–6Al–4V as built by selective laser melting, Mater. Sci. Eng. A. 768 (2019) 1–25. https://doi.org/10.1016/j.msea.2019.138456.
- [60] K. Artzt, T. Mishurova, P.-P. Bauer, J. Gussone, P. Barriobero-Vila, S. Evsevleev, G. Bruno, G. Requena, J. Haubrich, Pandora's Box–Influence of Contour Parameters on Roughness and Subsurface Residual Stresses in Laser Powder Bed Fusion of Ti-6Al-4V, Mater. . 13 (2020). https://doi.org/10.3390/ma13153348.
- [61] E. Wycisk, A. Solbach, S. Siddique, D. Herzog, F. Walther, C. Emmelmann, Effects of defects in laser additive manufactured Ti-6Al-4V on fatigue properties, Phys. Procedia. 56 (2014) 371–378. https://doi.org/10.1016/j.phpro.2014.08.120.
- [62] P. Edwards, M. Ramulu, Effect of build direction on the fracture toughness and fatigue crack growth in selective laser melted Ti-6Al-4 V, Fatigue Fract. Eng. Mater. Struct. 38 (2015) 1228–1236. https://doi.org/10.1111/ffe.12303.
- [63] B. Vayssette, N. Saintier, C. Brugger, M. El May, Surface roughness effect of SLM and EBM Ti-6Al-4V on multiaxial high cycle fatigue, Theor. Appl. Fract. Mech. 108 (2020) 102581. https://doi.org/https://doi.org/10.1016/j.tafmec.2020.102581.
- [64] K.S. Chan, M. Koike, R.L. Mason, T. Okabe, Fatigue life of titanium alloys fabricated by additive layer manufacturing techniques for dental implants, Metall. Mater. Trans. A Phys. Metall. Mater. Sci. 44 (2013) 1010–1022. https://doi.org/10.1007/s11661-012-1470-4.